Integrated Real-Time CMOS Luminescence Sensing and Impedance Spectroscopy in Droplet Microfluidics

Qijun Liu, *Student Member, IEEE*, Diana Arguijo Mendoza, *Student Member, IEEE*, Alperen Yasar, *Student Member, IEEE*, Dilara Caygara, *Student Member, IEEE*, Aya Kassem, Douglas Densmore, *Senior Member, IEEE*, and Rabia Tugce Yazicigil, *Senior Member, IEEE*

***Abstract*—High-throughput biosensor screening and optimization are critical for health and environmental monitoring applications to ensure rapid and accurate detection of biological and chemical targets. Traditional biosensor design and optimization methods involve labor-intensive processes, such as manual pipetting of large sample volumes, making them low throughput and inefficient for large-scale library screenings under various environmental and chemical conditions. We address these challenges by introducing a modular droplet microfluidic system embedded with custom CMOS integrated circuits (ICs) for impedance spectroscopy and bioluminescence detection. Fabricated in a 65 nm process, our CMOS ICs enable efficient droplet detection and analysis. We demonstrate successful sensing of luciferase enzyme-substrate reactions in nL-volume droplets. The impedance spectroscopy chip detects 4 nL droplets at 67 mm/s with a 45 pA resolution, while the luminescence detector senses optical signals from 38 nL droplets with a 6.7 nA/count resolution. We show real-time concurrent use of both detection methods within our hybrid platform for cross-validation. This system greatly advances conventional biosensor testing by increasing flexibility, scalability, and cost-efficiency.**

***Index Terms*—Impedance spectroscopy, bioluminescence detector, droplet microfluidics, synthetic biology, biosensors.**

Received 18 June 2024; revised 24 August 2024 and 11 October 2024; accepted 12 October 2024. Date of publication 7 November 2024; date of current version 17 December 2024. This work was supported in part by NSF SemiSynBio-II Program under Grant 2027045, in part by the Catalyst Foundation, in part by NIH T32 Training Program in Synthetic Biology and Biotechnology under Grant 1T32GM130546-01, in part by the Semiconductor Research Corporation (SRC) ESH Program (Task No.: 3245.001), and in part by NSF CAREER Program under Grant 2338792. This paper was recommended by Associate Editor A. J. Burdett. *(Qijun Liu and Diana Arguijo Mendoza contributed equally to this work.) (Corresponding author: Rabia Tugce Yazicigil.)*

Qijun Liu, Alperen Yasar, Dilara Caygara, and Aya Kassem are with the Department of Electrical and Computer Engineering, Boston University, Boston, MA 02215 USA.

Diana Arguijo Mendoza is with the Department of Biomedical Engineering, Boston University, Boston, MA 02215 USA.

Douglas Densmore and Rabia Tugce Yazicigil are with the Department of Electrical and Computer Engineering and the Department of Biomedical Engineering, Boston University, Boston, MA 02215 USA (e-mail: rty@bu.edu).

Color versions of one or more figures in this article are available at https://doi.org/10.1109/TBCAS.2024.3491594.

Digital Object Identifier 10.1109/TBCAS.2024.3491594

I. Introduction

HYBRID bio-electronic systems merge engineered cell-based biosensors (CBBs) with CMOS integrated circuits (ICs) to achieve biochemical sensing. These systems maintain high specificity and sensitivity in diverse applications, such as the human gastrointestinal (GI) tract [1], [2], wastewater treatment facilities [3], [4], bioreactors [5], and food safety monitoring [6], relying on CMOS ICs' stability for consistent operation and data communication, as depicted in Fig. 1(a). However, despite thorough assembly, characterization, and tuning, a biosensor may not perform as expected in real-world conditions since the effectiveness of biosensor screening methods may vary without considering all potential environmental variations in actual deployment scenarios [7].

Traditional biosensor optimization requires labor-intensive protocols, such as manual pipetting, extended cell culture incubation, and low-throughput well or agar plate assays (throughput of $\approx 10^4$ variants [8]), as shown in Fig. 1(b). While effective for small-scale experiments, these methods are inadequate for large-scale library screenings. In contrast, high-throughput screening (HTS) methods, capable of handling as many as 10^9 genetic variants [9], [10], are necessary in synthetic biology for categorizing extensive libraries and advancing protein and cell development.

Integrating microfluidic systems and biosensors can result in a powerful analytical tool offering real-time detection and rapid reaction times for optimizing and characterizing biosensors [11]. Microfluidics involves fluid manipulation at the sub-millimeter scale, making it well-suited for HTS because of its low reagent use, heightened sensitivity, and capacity for parallel processing. Their adaptability for point-of-care applications is notable, primarily due to portability [12]. However, conventional cell-based microfluidics is limited in efficiently screening biosensors for various environmental and chemical conditions. Droplet microfluidics [13], a specialized branch of microfluidics, excels in encapsulating cells or biochemical reactions in distinct droplets ranging from picoliters (pL) to nanoliters (nL) in volume, functioning as individual microreactors ideal for single-cell analysis [14], enzyme assays [15], and the generation of concentration gradients [16]. Further, pairing

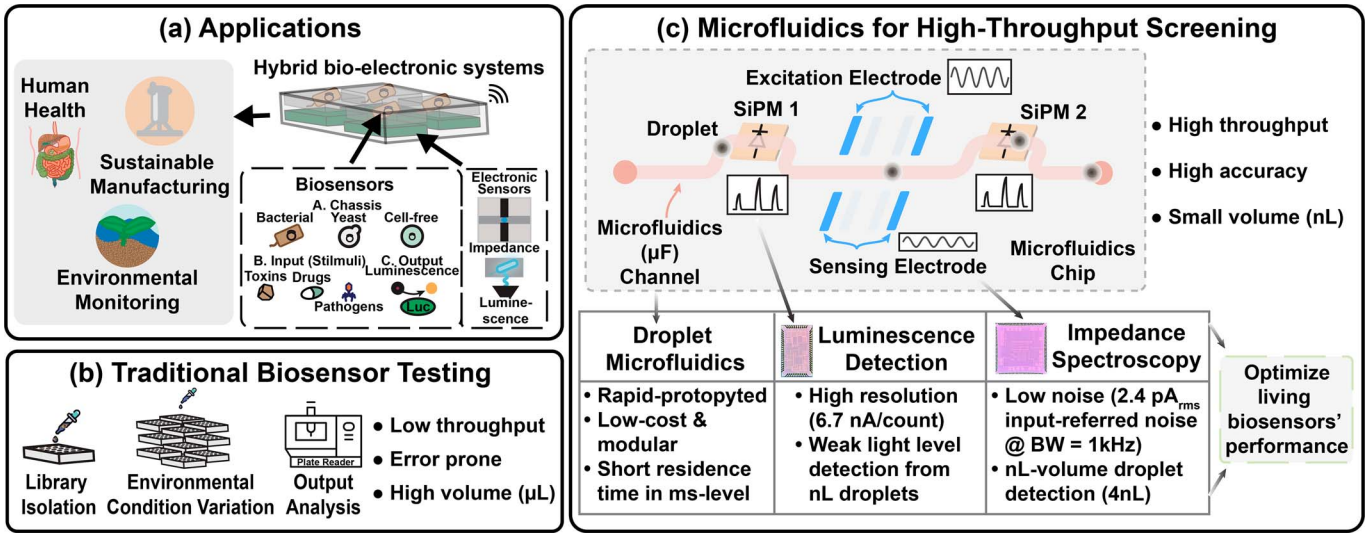

Fig. 1. (a) Applications of CMOS-integrated hybrid bio-electronic systems. (b) Traditional approach for biosensor screening and optimization. (c) Our proposed high-throughput droplet microfluidic platform with embedded CMOS sensors for impedance spectroscopy and luminescence sensing.

droplet microfluidics with automated fluorescence imaging has significantly enhanced screening capabilities, as it reduces optical cross-talk by compartmentalizing cells into droplets [17] and, therefore, considerably exceeding the scalability of conventional methods [18].

Although there have been significant advancements recently, droplet microfluidics still face challenges in achieving uniform droplet formation, precise manipulation, and efficient downstream processing [13]. Delays in data transfer from benchtop devices managing downstream processing exacerbate these issues. Scaling operations is an additional hurdle, as transitioning droplet-based processes to industrial scales requires maintaining efficiency and reducing errors. A trade-off between throughput and resolution ultimately persists, demanding a balance between the assay's detail and the processing volume within a given time frame. Custom CMOS ICs may be able to address these challenges effectively, offering scalable solutions for multiplexing and high-resolution, real-time sensing.

One potential method for enhancing the precision of droplet microfluidic systems lies in the use of luminescence as a biosensor reporter. Luminescence has been widely employed as a biosensor reporter across various applications [7], including the detection of water toxicity [19], heavy metals [20], and endocrine-disrupting compounds [21]. We employ luminescence over the more commonly used fluorescence, as it provides a power-efficient readout without the need for a light source or optical filters [22]. Despite its extensive use in the biosensor field, the integration of luminescent biosensors with high-throughput screening in droplet microfluidics has faced challenges. These challenges primarily stem from the difficulty in accurately sensing luminescence in droplets with low volumes, especially at high sample rates.

In this work, we present a modular droplet microfluidics (μF) system that encapsulates cells in water-based droplets inside oil-filled microfluidic channels, in conjunction with co-designed CMOS ICs, including impedance spectroscopy and bioluminescence detection. This system aims to harness the advantages of both droplet microfluidics and CMOS technology to enable rapid, high-throughput biosensor screening and optimization under diverse environmental and chemical conditions. This approach aims to improve biosensor performance, ensuring adherence to the required sensitivity, specificity, and robustness standards for particular applications.

Fig. 1(c) illustrates a high-throughput droplet microfluidic platform with integrated CMOS impedance spectroscopy and luminescence detection. By combining these two modalities, this approach enables comprehensive analysis by cross-validating droplet generation parameters, such as size and speed, through impedance measurements, while simultaneously capturing critical information about luciferase enzyme-substrate reactions via luminescence detection. This dual-modality approach is particularly advantageous in complex scenarios where cell populations exhibit intricate relationships with expression levels, facilitating more accurate cell-density normalization and ultimately optimizing the design of living biosensors.

Our work introduces the first co-design of high-throughput droplet microfluidics with integrated CMOS luminescence and impedance sensors, exemplified by successfully detecting luciferase enzyme reactions within nL-volume droplets [23]. The high-resolution impedance spectroscopy chip detects droplets (4 - 47.9 nL) at a maximum velocity of 67 mm/s, with a sensitivity of 45 pA and multiple gain configurations, utilizing a pseudo-resistor-based transimpedance amplifier (TIA) feedback network. Concurrently, our custom-designed luminescence detector chip, connected to commercial silicon photomultipliers (SiPMs), accurately measures optical signals from bioluminescent droplets (minimum droplet volume at 38.2 nL) and 125 nL microfluidic channels containing NanoLuc.

This article is organized as follows: Section II presents the overall system architecture and key features. Section III discusses the circuit-level implementation and analysis of

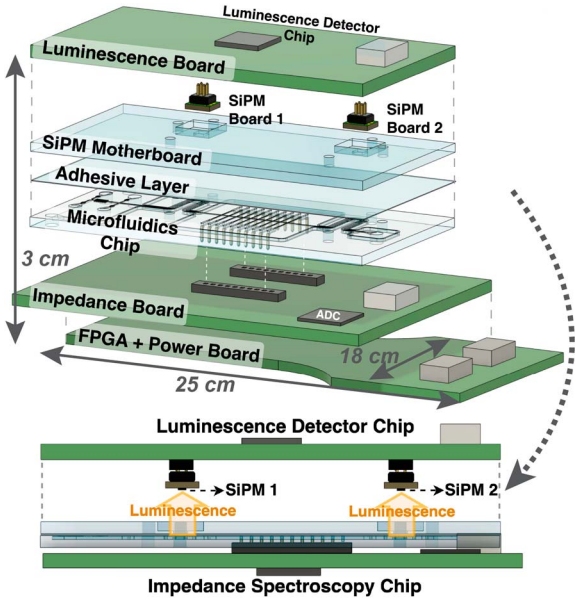

Fig. 2. 3D rendering of the co-designed modular platform technology.

the impedance spectroscopy and luminescence sensor chips. The measurement setup and results are presented in Section IV, followed by the conclusions in Section V.

II. Co-Design of Droplet Microfluidics and CMOS-Integrated Sensors

The following sections provide details on the motivation and innovation behind our co-designed droplet microfluidics system with embedded CMOS sensors. This system integrates CMOS bioluminescence detection and impedance spectroscopy, as shown in Fig. 2. We discuss recent advancements in droplet microfluidics, focusing on our use of CNC micromilling to fabricate precise microfluidic devices from low-cost thermoplastics, thus avoiding traditional fabrication costs and complexity. Our approach streamlines the design and fabrication of microfluidic devices shown in Fig. 3 by incorporating readily available conductive-ink electrodes and utilizing techniques to reduce optical cross-talk for SiPM integration, such as designing a loop channel filled with light-blocking black oil. Additionally, we delve into the important co-design parameters of droplet microfluidics and electronics. Finally, this section concludes with a discussion on the necessity of integrating impedance and luminescence sensing in this hybrid platform technology, which enhances data reliability and provides comprehensive insights into biological analysis and biosensor performance characterization.

A. CNC-Micromilled Droplet Microfluidic Devices

Microfluidic technology is constrained by the complexity and cost of fabricating polydimethylsiloxane (PDMS) devices, which require cleanroom facilities and are difficult to scale due to the time-consuming prototyping process [24]. The use of thermoplastics like polycarbonate for microfluidic device fabrication presents a practical solution, simplifying the scaling process by reducing costs and manual labor [24], [25], [26].

To circumvent conventional manufacturing challenges, researchers have explored rapid prototyping techniques, such as laser cutting [27], [28], [29], 3D printing [30], [31], [32], and micromilling [33]. Laser cutting offers precise substrate etching, but its effectiveness is limited by the compatibility constraints with certain thermoplastics (e.g., polycarbonate and polyvinyl chloride) and the risk of material leaching, which can adversely impact biological reactions [34]. Conversely, 3D printing introduces novel fabrication methods but is often hindered by issues related to substrate compatibility (e.g., transparency) [35] and feature size constraints (100 μm) [36], posing challenges for high-throughput screening.

In this work, we focus on a desktop-scale Computer Numerical Control (CNC) micromilling approach that substantially reduces both the time ($<$ 1 hour) and the cost ($<$ \$10) [37] required for the fabrication of droplet-based microfluidic devices on thermoplastics, including polycarbonate, acrylic, and polymethyl methacrylate (PMMA) [33]. This approach permits the rapid prototyping of devices with precise features down to 50 μm, facilitating comprehensive experimental design investigations within limited budgets and time frames [37].

The methodology entails generating G-code via CAD design tools (e.g., SolidWorks, AutoCAD), which a CNC micromill employs to engrave device geometries onto thermoplastic substrates [37]. During micromilling, maintaining precise feed and speed rates is imperative to avert the breakage of small endmills. After milling, devices undergo deburring to guarantee smooth fluid dynamics. They are then assembled using double-sided adhesive and sealed with an additional polycarbonate layer, forming the microfluidic device shown in Fig. 2.

Furthermore, unlike the inherent hydrophobic nature of PDMS, polycarbonate microfluidics require surface treatment to coat the channels in a hydrophobic material, which is essential for the generation of droplets within fluorinated oil-filled microfluidic channels [38]. Fluorinated oils are preferred in biological applications due to their compatibility with organic materials and capacity for oxygen transport [39]. A comprehensive multi-stage treatment process, incorporating Aquapel, air expulsion, and thermal curing, secures the device's long-term hydrophobic stability for sustained droplet production [40].

B. Conductive-Ink Electrodes and SiPM Integration

Electrode integration is used for impedance sensing in droplet microfluidic platforms. This sensing is achieved by aligning electrodes on opposing sides of the microfluidic channel, quantifying the impedance profile between the electrodes through the measurement of input current at the sensing electrode when an AC voltage is applied to the excitation electrode. This enables the monitoring of droplet characteristics, such as position, size, and velocity, alongside complex biological properties, including cellular differentiation and genomics content [41].

We integrate electrodes in micromilled microfluidic devices compatible with dead-end filling. This process allows electrodes to function without a continuous path from input to output, making it ideal for two-electrode systems placed on

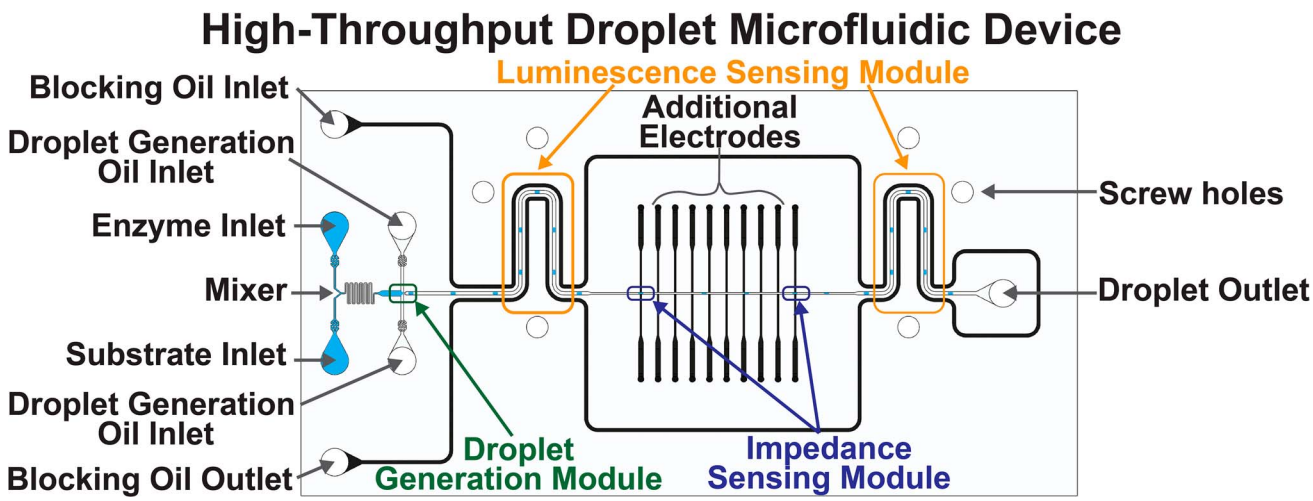

Fig. 3. Droplet microfluidics device with modular droplet generation, impedance sensing, and luminescence sensing.

opposite sides of a channel, thereby streamlining the architecture of droplet microfluidic devices [42]. Traditional techniques for electrode integration, including metal vapor deposition, are often not scalable, necessitate exact alignment, or fail to accommodate dead-end configurations [43]. Conversely, saltwater electrodes are economical but require gas-permeable materials and a constant connection to reservoirs (e.g., microfluidic channel) and high voltage electronic circuitry, which constrains their application [44].

In this work, a novel electrode-integration technique is employed that uses readily available carbon-based conductive ink to address these limitations. This ink is more cost-effective and easier to apply than metal-based alternatives but also provides higher conductivity than saltwater and can fill dead-end electrodes [42]. The procedure entails etching channels into a substrate for electrodes, in addition to fluid paths, applying conductive ink and removing excess with isopropyl alcohol, and connecting the electrodes to CMOS chips through 90° gold pin headers. This technique enables quick manufacturing turnaround within a single day.

In addition, our platform utilizes commercial SiPM components with a defined area of $1 \times 1\ mm^2$. The incorporation of SiPM devices into the microfluidic platform involves milling the footprint of the SiPMs into a polycarbonate layer, which is then placed atop the primary microfluidic layer, as illustrated in the side view of the 3D rendering of this platform (Fig. 2). To achieve high detection accuracy from a single droplet within the sensing area of the SiPM, we developed a horse-shoe microfluidic channel configuration (Fig. 4). This channel, which utilizes light-blocking black oil, plays a crucial role in our system. It prevents the luminescence of peripheral droplets from affecting the bioluminescence detection, reducing the optical cross-talk from neighboring droplets.

C. Droplet Microfluidic Device Parameters

This work focuses on two primary droplet parameters for identification and quantification: the droplets' size and

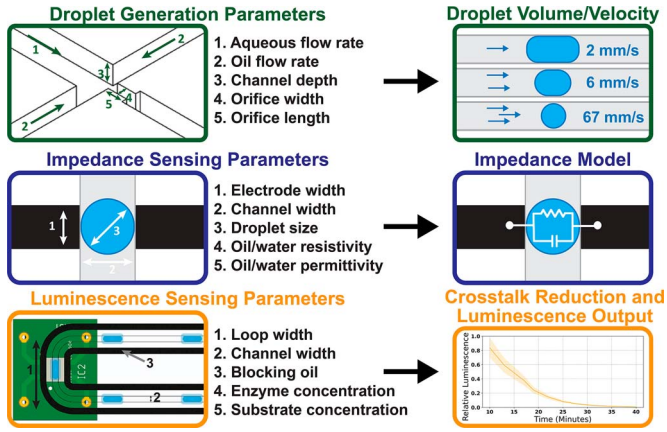

Fig. 4. Droplet microfluidics device parameters for droplet generation, impedance sensing, and luminescence sensing.

residence time over the sensing area (either the electrodes' sensing zones or the SiPM's detection region), as shown in Fig. 4.

Practically, to determine droplet size, it is necessary to establish the droplet generation rate. The rate can be determined by employing a peak detection algorithm on the impedance readout from benchtop instruments (e.g., LCR meter) and counting the signal peaks over a specific duration. Alternatively, if the LCR meter fails to detect rapid droplet events, a high-speed camera is utilized to enumerate droplets over a designated time frame. By combining the droplet generation rate (r_D) with the volumetric water flow rate (Q_w), we can calculate the average droplet diameter (d) using Eq. 1 [45]:

$$d = 2\left(\frac{3Q_w}{4r_D\pi}\right)^{1/3} \tag{1}$$

The residence time (t_r) of droplets within the sensing region is a function of the sensor width (W_S), channel width (W_C), channel depth (D_C), and the total volumetric flow rate (Q_T), or the droplet volume (V) and total volumetric flow rate (Q_T),

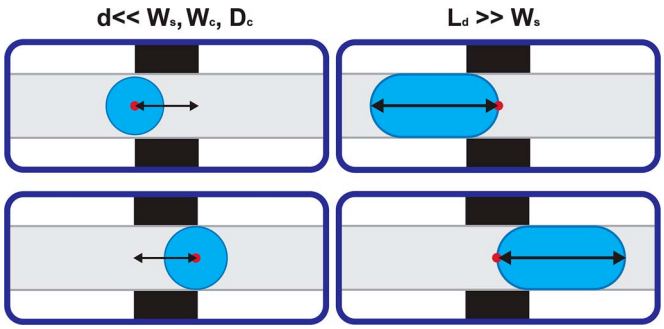

Fig. 5. Droplet residence time in sensing area for spherical vs. larger droplets.

contingent upon the droplet diameter (d) and length (L_D). If the droplet shape is spherical, the diameter d is used; however, for larger droplets where the "diameter" exceeds the sensing region's width, the length L_D is considered, as depicted in Fig. 5 and described by Eq. 2. The optimal sampling frequency is derived from the residence time based on the requisite number of samples for averaging to improve the signal-to-noise ratio (SNR).

$$t_r = \begin{cases} \frac{W_S W_C D_C}{Q_T}, d << W_S, W_C, D_C \\ \frac{V}{Q_T}, L_D >> W_S \end{cases} \tag{2}$$

D. Multimodal Sensing With Impedance and Luminescence

Simultaneous impedance and luminescence assessments significantly enhance the analysis of biological and chemical systems [46]. Multimodal sensing is employed for cross-validation, thereby improving the overall accuracy and reliability of the data. For instance, in CMOS-integrated droplet microfluidics, impedance sensing monitors the internal environment of each droplet, detecting the presence and concentration of cells or biomolecules by measuring changes in the electrical properties of the droplet contents. Concurrently, luminescence sensing can report on activity within the droplet, such as enzyme reactions or gene expression, by detecting light emission from reporter molecules.

Furthermore, combining bioluminescence detection with impedance-based cell density normalization provides an in-depth system analysis by determining if an observed light signal is generated because of a small number of cells with high protein expression or many cells with weak expression. Such differentiation is vital for accurately characterizing sensor performance in biosensing applications.

III. Circuit and System Implementation

Here, we discuss the circuit and system implementation details and the design decisions underpinning the high sensitivity and resolution in real-time impedance spectroscopy and luminescence detection. The chips were fabricated using 65 nm CMOS technology. The analog circuit blocks employ core devices with the standard threshold voltage, whereas the synthesized digital circuit blocks utilize high-threshold voltage devices to minimize the leakage current.

A. Impedance Spectroscopy Architecture

The impedance spectroscopy chip features two identical impedance sensing channels, enabling data averaging and cross-validation. The impedance spectroscopy front end comprises a coherent in-phase (I) and quadrature-phase (Q) receiver as shown in Fig. 6. This receiver includes a high-gain transimpedance amplifier (TIA) with a feedback network formed by a temperature- and process-compensated pseudo-resistor, offering variable gain via a pseudo-current mirror. It also uses a passive mixer, actuated by 25%-duty-cycle quadrature local oscillator (LO) signals, second-order passive low pass filters (LPFs) with adjustable bandwidths, and variable-gain amplifiers (VGAs). A four-transistor voltage reference [47] generates the TIA and VGA's common-mode voltage (VCM).

1) Operation Principle of Impedance Spectroscopy: In real-time, the impedance spectroscopy is designed to measure the admittance between two conductive ink electrodes, represented by $Y(\omega_1)$. When a sinusoidal excitation voltage signal $V_{exc}(\omega_1)$ is applied to the excitation electrode, the resulting current through the sensing electrode, $I(\omega_1)$, is measured. Subsequently, the admittance seen by the electrode pair is calculated using Eq. 3.

$$Y(\omega_1) = \frac{I(\omega_1)}{V_{exc}(\omega_1)} \tag{3}$$

As all signals in the system are sinusoidal, determining $Y(\omega_1)$ requires calculating the sensing current's relative amplitude and phase shift compared to the excitation voltage $V_{exc}(\omega_1)$. We employed coherent detection techniques, a standard topology in traditional receivers known as the direct conversion architecture, to acquire the phase and amplitude information of the sensing current $I(\omega_1)$. As illustrated in Fig. 6, this current ($I(\omega_1)$) is amplified using a low-noise TIA with a gain determined by a feedback pseudo-resistor. The TIA's output is then multiplied by 25%-duty-cycle local oscillator signals (I, In, Q, and Qn) at the frequency ω_2. Low-pass filters eliminate the higher-order harmonics resulting from the mixing process. The differential to single-ended VGA consolidates the bipolar $I'' - In''$ and $Q'' - Qn''$ signals into I_FINAL ($V_I(\omega_1 - \omega_2)$) and Q_FINAL (($V_Q(\omega_1 - \omega_2)$) outputs and applies additional gain. The amplitude of the I and Q channels, denoted by V_I and V_Q respectively, can then be used to estimate $Y(\omega_1)$'s amplitude and phase using Eq. 4 and Eq. 5, respectively. A in Eq. 4 represents the overall gain of the system, including TIA gain, LPF loss, and VGA gain.

$$|Y(\omega_1)| = \frac{\sqrt{V_I^2 + V_Q^2}}{A \cdot |V_{exc}(\omega_1)|} \tag{4}$$

$$\angle Y(\omega_1) = tan^{-1}\left(\frac{V_Q}{V_I}\right) \tag{5}$$

2) Impedance Model: Impedance models are used for simulation to establish the front-end circuit specifications, including

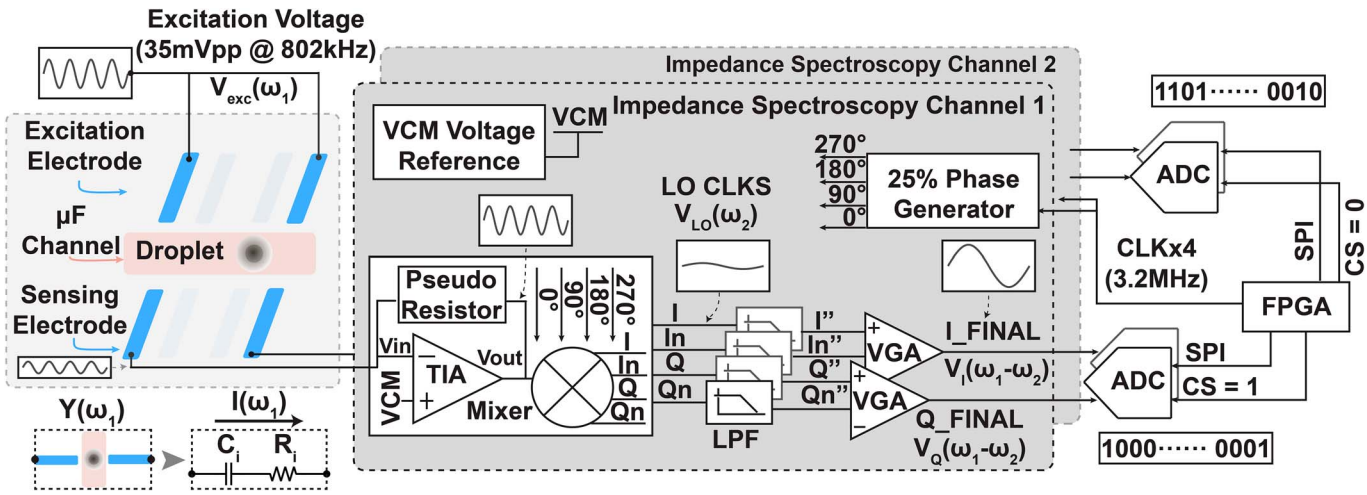

Fig. 6. Impedance spectroscopy receiver architecture.

TIA and VGA gains and TIA bandwidth. Numerous factors influence the impedance, including the design of the microfluidic device and its interface with the CMOS impedance spectroscopy chip. For example, variations in the widths of the microfluidic channel and electrodes can significantly affect impedance; a narrower channel increases the baseline impedance, while a wider channel decreases it (Fig. 4).

We initially measured the impedance of aqueous droplets and oil using an LCR meter (E4980A, Keysight Technologies) across various microfluidic devices, excitation voltages, and excitation frequencies (f_1) to determine the expected range of impedance. The LCR meter provides a simple model represented as a series-connected capacitor (C) and resistor (R), although the impedance model may be more complex. Aligning with the LCR meter results, we adopt this simplified impedance model as illustrated in Fig. 6, representing the inverse of the expected admittance as measured by the CMOS chip given by Eq. 6.

$$|Z(\omega_1)| = \sqrt{R_i^2 + \left(\frac{1}{2\pi f_1 C_i}\right)^2} = \sqrt{R_i^2 + \left(\frac{1}{\omega_1 C_i}\right)^2} = \frac{1}{|Y(\omega_1)|} \tag{6}$$

As the excitation frequency decreases, the impedance increases, posing challenges for the front-end circuits, which must provide higher gain to amplify the small input current $I(\omega_1)$. Although the LCR meter accurately measures up to 1 MHz, we selected an 800 kHz excitation frequency to ensure reliable impedance modeling from the LCR meter and to facilitate a less demanding front-end design due to the lower impedance value obtained than applying a lower excitation frequency.

Preliminary measurements using an LCR meter at 800 kHz indicate that the water droplet exhibits a capacitance of 62.5 fF and a resistance of 22.5 kΩ (total impedance of 3.18 MΩ). In contrast, the oil-filled microfluidic channel presents a capacitance of 61.9 fF and a resistance of 22.2 kΩ (total impedance of 3.21 MΩ). With an excitation voltage of 20 mV, this results in an input current difference of approximately 59 pA. To ensure that our system can reliably detect this difference and achieve the necessary sensitivity, the TIA must have a minimum gain within the MΩ range. Notably, the impedance is predominantly capacitive, aligning with the high intrinsic impedance of the polycarbonate substrate used in our microfluidic devices. Furthermore, the capacitive dominance means that the phase variation between water and oil droplets is minimal; thus, our system measurements discussed in Section IV-C concentrate only on the impedance magnitude.

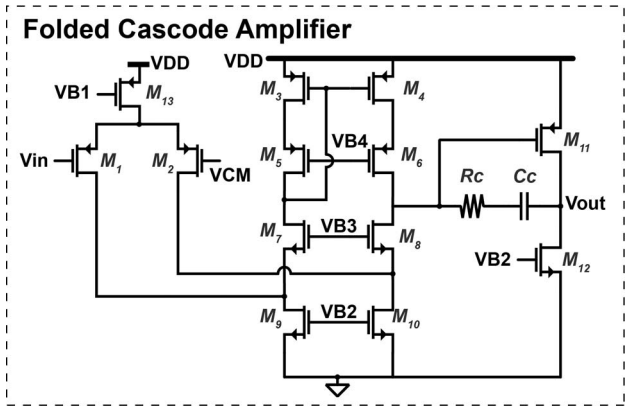

Fig. 7. Folded cascode amplifier implementation used in transimpedance amplifier.

3) Transimpedance Amplifier With a Pseudo-Resistor Feedback Network: Apart from providing amplification, the main purpose of the low-noise and high-gain TIA is to maintain a low-impedance node at the sensing electrode contact. This ensures that $Y(\omega_1)$ remains directly proportional to the measured variable and is not affected by the TIA's input impedance [48]. The TIA consists of a two-stage folded cascode amplifier with PMOS input pairs (Fig. 7), biased using current mirroring from a corresponding folded cascode bias circuit shown in Fig. 8. Post-layout simulations show that the TIA achieves an open-loop gain of 79 dB and a unity-gain bandwidth of 39 MHz at a

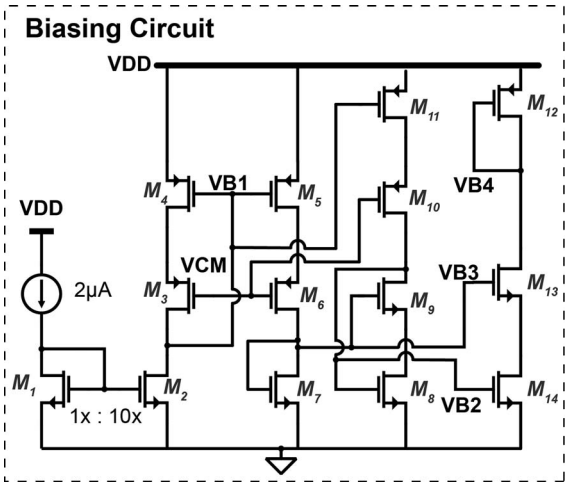

Fig. 8. Bias circuit of the transimpedance amplifier.

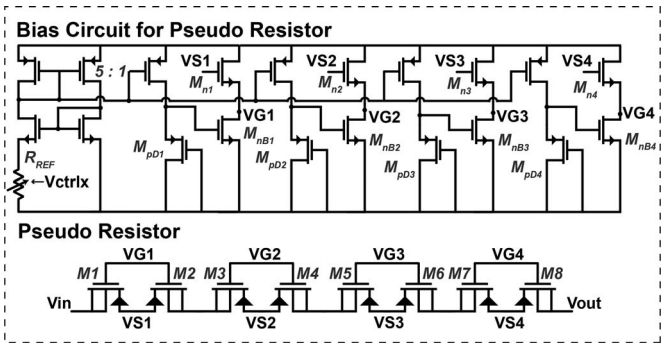

Fig. 9. Temperature- and process-compensated pseudo-resistor implementation.

typical corner, supporting a theoretical 3dB bandwidth of 1.39 MHz, which allows for accurate measurement of excitation frequencies up to our target of 1 MHz, while consuming 233 μW of power from a 1.2 V supply voltage. A large input pair size (M_1 and M_2 in Fig. 7) of $W/L = 340.8/0.4$ is used to minimize flicker (1/f) noise. The second stage of the amplifier provides a high swing and delivers the requisite low output impedance to drive the feedback resistor. Additionally, it incorporates Miller compensation (R_c and C_c) for improved stability.

The traditional three-terminal P+ poly resistors without silicide can provide stable resistance up to the Megaohm range. However, due to their large size, they require more area and introduce significant parasitic capacitances that can negatively impact the stability of the TIA. Fig. 9 shows the pseudo-resistor-based feedback network, which is crucial for achieving the high feedback resistance (7.6, 14.4, or 24.8 $M\Omega$) that our system needs. This pseudo-resistor implementation uses four pairs of PMOS devices (M1 to M8) connected in series [49], with the body terminal connected to the drain, to enhance resistivity through the body effect [50]. The four-stage configuration reduces the voltage drop across each PMOS pair, thereby improving the linearity of the pseudo-resistor feedback. The current biasing of the pseudo resistor enables variable gain control via

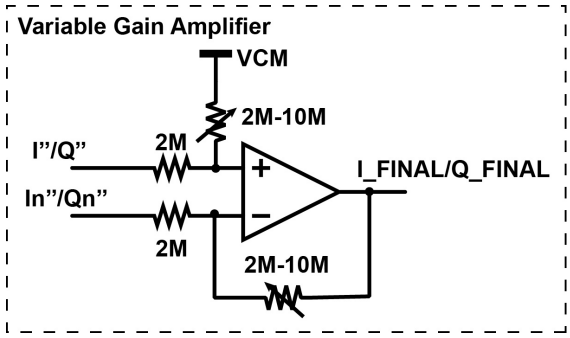

Fig. 10. Variable-gain amplifier implementation.

the V_{ctrlx} signals. These signals, which can be programmed through the digital configuration block, allow for the selection of different resistor values R_{ref}. As a result, the current through the current mirroring branch can be adjusted, thereby altering the pseudo-resistor biasing values (V_{G1} to V_{G4}) [49]. In this design, the W/L ratio for M_{pDx} is less than one, favoring a longer device length over width to enhance the pseudo-resistor's bandwidth and, consequently, the front-end circuit stability.

4) Passive Mixer, LPF, and Differential-to-Single-Ended VGA: The output voltage V_{out} from the TIA is converted to baseband signals I, I_n, Q, and Q_n using a 4-phase passive mixer driven by 25%-duty-cycle quadrature LO signals at ω_2. This results in baseband signals with a frequency of $|\omega_2 - \omega_1|$.

After the passive mixer, second-order passive LPFs are used to maintain low power consumption. These LPFs have a tunable bandwidth ranging from 15 kHz to 35 kHz, achieved by utilizing digitally programmable capacitance values in the RC networks to effectively attenuate higher-order harmonics with a 40 dB/dec roll-off.

In addition, a programmable VGA (Fig. 10) with digitally adjustable gain from 0 to 14 dB is incorporated to enhance the receiver's sensitivity. The VGA employs a biasing scheme similar to the TIA bias circuit, with the current mirror's ratio set at 1 to 8.6.

5) Common-Mode Voltage Reference and 25% Phase Generator: The VCM reference uses a 4-transistor voltage reference design based on [47]. This VCM reference is adjustable, allowing for switching between different transistor sizes to accommodate variations in process corner and temperature.

The 25% duty-cycle phase generator follows the structure presented in [22]. The input CLK is typically set to $4\omega_1$ to ensure that the baseband signals align with the DC component after downconversion. When the DC voltage VCM is present at the baseband, it becomes difficult to isolate the downconverted baseband signals if they also exist at the DC level. It is common to set the $CLK = 4\omega_2$ different from $4\omega_1$ so that after downconversion, the resulting signals have a frequency of $|\omega_1 - \omega_2|$. This simplifies the retrieval of amplitude information necessary for back-calculating $Y(\omega_1)$.

B. Bioluminescence Detector Architecture

The system features a dual-channel luminescence detector that processes the light pulse amplitude of the commercial SiPM

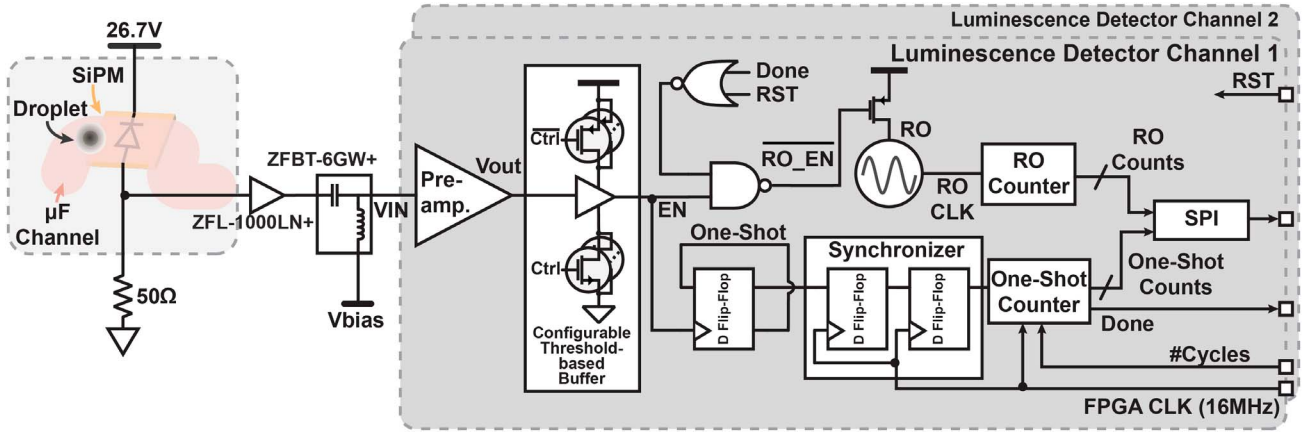

Fig. 11. Luminescence detector architecture.

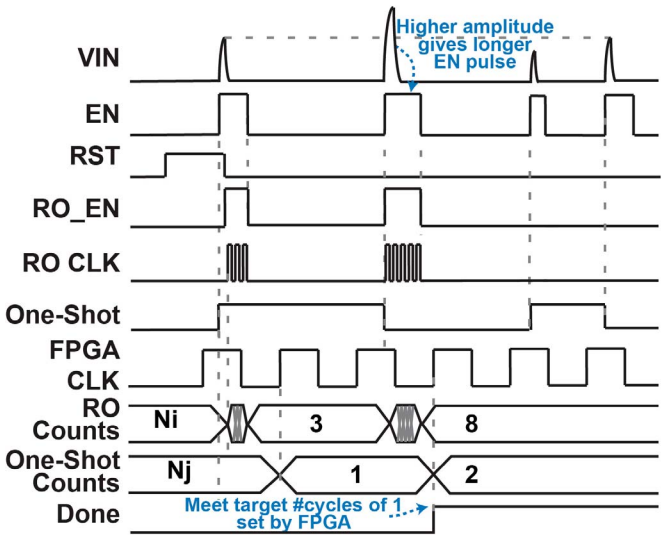

Fig. 12. Timing diagram showing the operation of luminescence sensing for different amplitudes and frequencies of SiPM light pulses.

using a ring-oscillator-driven (RO-driven) counter and pulse frequency through a one-shot counter, illustrated in Fig. 11.

1) Operation Principle of Luminescence Detector: The timing diagram in Fig. 12 illustrates the operations of the bioluminescence detector. The commercial SiPM, with a gain of 2×10^5, produces high-frequency, high-amplitude pulses when the light intensity increases. Traditional one-shot counters typically use pulse frequency for photon detection. However, in the case of nL-volume droplets with lower luminescence, the pulse amplitude domain more accurately encodes the luminescence level.

When the cumulative current (I_{MAX}) generated by photons activates a higher number of microcells in the SiPM, it results in a larger pulse amplitude of V_{IN}. Consequently, this leads to an extended pulse width for the EN signal generated by the custom threshold-crossing-based buffer, shown in Fig. 12. The increased EN pulse width enables the RO counter for additional cycles, thus updating the $RO\,Counts$. In contrast to the RO counter, the one-shot counter does not respond to the amplitude increase of VIN. Instead, it counts the rising edges of VIN and EN independently of their amplitude and width. Once the one-shot counter reaches the predefined cycle count specified by the user, it triggers the $DONE$ signal, which stops the RO counter chain. The $DONE$ signal is connected as an input to the FPGA, which continuously monitors the signal. When the $DONE$ signal goes high, the FPGA reads data from both counters via the on-chip SPI.

2) Silicon Photomultiplier Model: A Single-Photon Detector (SPD) refers to any device capable of detecting individual photons, including Single-Photon Avalanche Diodes (SPADs). In contrast to Avalanche Photodiodes (APDs), which operate just below the breakdown voltage, SPADs function above the breakdown voltage in Geiger mode [51]. This mode allows them to produce a large, self-sustained avalanche for each detected photon, resulting in high sensitivity. Silicon Photomultipliers (SiPMs) are photodetectors made up of an array of SPADs, also known as microcells or pixels. Each microcell operates independently and is connected in parallel. These cells are typically square-shaped, with edge lengths ranging from 10 to 100 μm [52]. SiPMs convert light into electrical current without the need for a vacuum tube to amplify the signal. Compared to traditional photomultiplier tubes, SiPMs are more compact, robust, and energy-efficient, while offering higher gain than individual SPADs. This makes them suitable for portable and miniaturized devices requiring fast timing [53], [54]. SiPMs are often used in applications that involve detecting low-light intensities, such as light detection and ranging (LIDAR) [55], [56], functional optical spectroscopy [57], [58], [59], and fluorescence detection in biological and physics research [60], [61]. SiPMs also have applications in quantum physics [62] and quantum informatics [63]. Looking ahead, integrating SiPMs with CMOS technology holds potential for even more compact and energy-efficient designs [64], [65].

Fig. 13 illustrates the electrical circuit model of the SiPM for this work. In this schematic, n_f represents the number of activated microcells out of the total number of microcells (n_t) available in the SiPM, leaving $n_t - n_f$ as the count of inactive

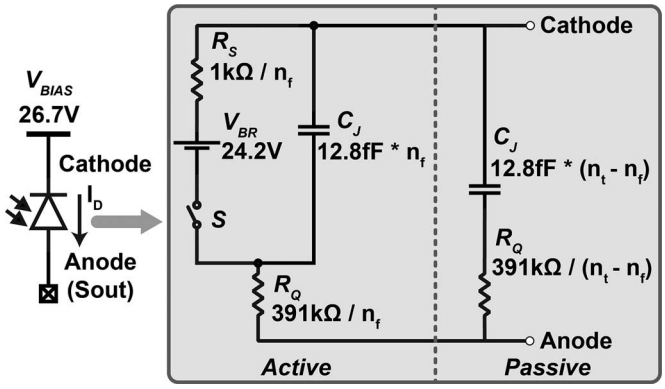

Fig. 13. Equivalent electrical circuit model of the SiPM.

cells. S refers to a virtual switch used for modeling purposes, which closes during the quenching process.

Under dark conditions and ignoring dark noise, the switch S remains open, allowing the capacitor C_J to charge up to the bias voltage V_{BIAS}. S is closed when a photon is detected, causing C_J to discharge through the resistor R_S. With the SPAD biased by a constant voltage source, V_{BIAS}, current flows through the circuit, resulting in a steady-state current I_D given by Eq.7. V_{OV} is the overvoltage defined as $V_{BIAS} - V_{BR}$, where V_{BR} is the breakdown voltage.

$$I_D = V_{OV}/R_S \tag{7}$$

The avalanche initiation causes the current through the cathode terminal to increase, characterized by a time constant given by Eq. 8. The recovery time constant, τ_r, typically spans tens of picoseconds.

$$\tau_r = C_J \cdot R_S \tag{8}$$

Quenching occurs when the current I_D reaches a self-sustaining maximum level, denoted as I'_{MAX} (Eq. 9). This leads to the recharging of C_J back to the nominal voltage V_{BIAS}. Then, I_D decreases over the recharge time constant $\tau_{recharge}$ given by Eq. 10.

$$I'_{MAX} = \frac{V_{OV}}{R_Q + R_S} \tag{9}$$

$$\tau_{recharge} = C_J \cdot R_Q \tag{10}$$

In the initial stage of recharging, the current is sourced not just from V_{BIAS} but also from the junction capacitors of neighboring pixels. SiPMs enable photon counting via two approaches: via digital, where each SPAD is connected to a distinct readout circuit [66], and via analog, through the assessment of the overall signal amplitude [67].

In this bioluminescence detection system, employing a commercial SiPM limits access to individual SPADs, necessitating analog processing of photon counts due to exclusive access to the SiPM's anode or cathode. The utilized commercial SiPM (microFC-10010-FC by OnSemi) comprises 2880 microcells, each with dimensions of $10 \times 10\ \mu m^2$, covering a total area of $1 \times 1\ mm^2$. The datasheet specifies a SiPM gain of 2×10^5 with a microcell recharge time constant of 5 ns at an overvoltage (V_{OV}) of 2.5 V. To align with performance specifications (e.g., dark current, anode-cathode capacitance, and gain), an overvoltage of 2.5 V was applied in addition to the minimum breakdown voltage (V_{BR}) of 24.2 V, setting the bias voltage at 26.7 V. The junction capacitance (C_J) is calculated based on the SiPM's gain using Eq. 11, while the quenching resistor (R_Q) is estimated from the recharge time constant using Eq. 12.

$$C_J = \frac{Gain \cdot q}{V_{OV}} = 12.8fF \tag{11}$$

$$R_Q = \tau_{recharge}/C_J = \frac{5 \times 10^{-9}}{12.8 \times 10^{-15}} \approx 391\ k\Omega \tag{12}$$

Quantifying the series resistance (R_S) poses a challenge, yet it is assumed to be relatively low, typically is in the $k\Omega$ range. Simulations have shown that variations in R_S across a broad spectrum minimally impact the model's output, given that R_S is substantially lower than R_Q [68].

Again, Eq. 9 indicates that the maximum photocurrent I'_{MAX} produced by a single pixel does not depend on the intensity of light but is exclusively defined by the electrical properties of the individual microcell. Upon exposure to light, a multitude of photons are expected to trigger several microcells. With the increase in the number of active microcells, the aggregate peak current (I'_{MAX}) contributed by each cell escalates, leading to a heightened overall current I_{MAX} in the SiPM.

3) Preamplifier and Configurable Threshold-Crossing-Based Buffer: As recommended by the datasheet, we connect a 50 Ω series resistor to the commercial SiPM's standard output ($Sout$, also known as the anode port). The SiPM cathode is connected to the bias voltage supplied by a DC power source and is coupled with a 10 nF decoupling capacitor to prevent DC voltage drops caused by SiPM quenching.

The avalanche pulses at the Sout node are processed using a commercial pre-amplifier (ZFL-1000LN, Mini-Circuits) with a 20 dB gain and a bias tee (ZFBT-6GW+, Mini-Circuits) that isolates the high voltage from the 26.7 V SiPM bias voltage and establishes an input DC voltage of 570 mV. VIN represents the actual signal fed into the chip. This signal undergoes further amplification on the chip through a three-stage pre-amplifier consisting of two self-biased amplifiers and a differential to single-ended VGA, as depicted in Fig. 14. The three-stage pre-amplifier with a 3 dB bandwidth of 36 MHz provides an additional gain of 28 dB.

The amplified output, $Vout$, from the pre-amplifier is fed into a configurable threshold-crossing-based buffer to produce the EN signal for subsequent amplitude-to-digital conversion processes. Using the configurable threshold-crossing buffer instead of a standard library buffer ensures consistent performance across process variations and supports the functionality of following circuit stages.

Since the SiPM's recharge duration is primarily dictated by the junction capacitance (C_J) and the quenching resistance (R_Q), an increased peak current, I_{MAX}, triggered by a specific light intensity, requires more time for $Vout$ to fall and reach the buffer's threshold voltage. This prolongs the pulse duration

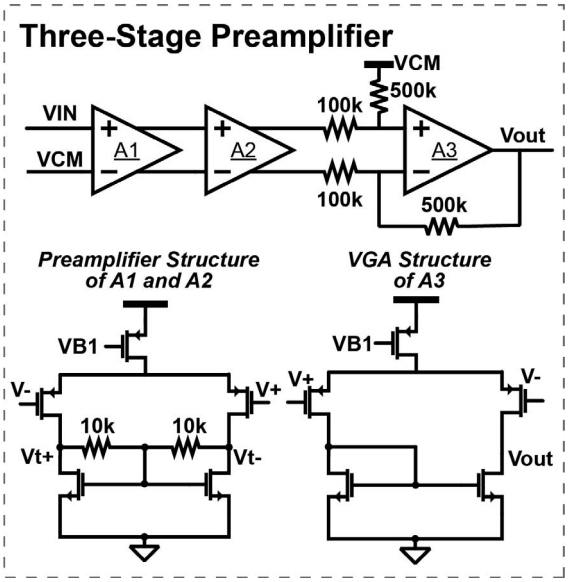

Fig. 14. Three-stage pre-amplifier implementation.

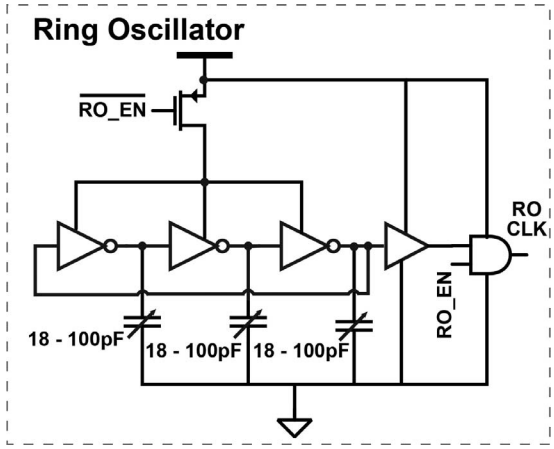

Fig. 15. Ring oscillator implementation.

of the enable signal EN. The threshold voltage for the configurable buffer can be set within a range of 570 to 600 mV.

4) One-Shot Counter: The device has a one-shot counter (Fig. 11) that is designed to record avalanche spikes. This counter detects the rising edge of the EN signal and extends the period using a D-flip flop scheme to allow counting of clock cycles from a faster clock. In this work, the faster clock is a 16 MHz signal provided by the FPGA. This technique is commonly used in digital SiPM sensors for time-to-digital conversion [69], [70]. The counting process stops when the FPGA determines that a predefined number of cycles have been completed, and the $DONE$ signal is triggered at this point. When the expected optical power increases, causing more frequent avalanche spikes, the one-shot counter stops early, resulting in fewer counts.

5) Ring-Oscillator-Driven Counter: The EN signal functions as an activation switch for the RO shown in Fig. 15. A wider pulse width of EN results in more cycles of the $ROCLK$ signal. A digital synthesis counter accumulates the rising edges of $ROCLK$ until it is stopped by the $DONE$ signal from the one-shot counter. By incorporating a digital programmable capacitor array within the RO, frequency adjustments ranging from 200 MHz to 1 GHz can be achieved in simulation, ensuring reliable performance despite process variations. Additionally, an AND gate placed at the final stage of the RO ensures that $ROCLK$ is promptly reset to zero once EN is deactivated.

In this work, nL-volume droplets exhibit luminescence at an intensity comparable to the dark count level, resulting in a very low SNR. The VIN captures original photon spikes from luminescence but also includes dark counts, digital clock feed-through from the printed circuit board (PCB), and noise. As the increase in pulse amplitude is directly linked to light intensity, representing the luminescence more accurately in the pulse amplitude domain is essential. Therefore, the RO counter offers a more precise assessment of bioluminescence intensity for our specific application.

IV. Measurement Results

In this section, we first discuss the integration of our hybrid platform that combines impedance spectroscopy and luminescence detector chips fabricated in 65 nm CMOS technology. Next, we present the electrical performance characterization of the impedance spectroscopy chip and demonstrate real-time droplet detection using our droplet microfluidic platform embedded with impedance spectroscopy. Then, we discuss the electrical and optical performance characterization of the luminescence detector chip, showcasing its real-time sensing capability for the NanoLuc luciferase enzyme-substrate reaction, as well as the detection of bioluminescent droplets formed by *Escherichia coli* (*E. coli*) with the NanoLuc gene and their interaction with the substrate. Finally, we present a real-time sensing measurement demonstrating the concurrent use of impedance spectroscopy and luminescence detector chips within our hybrid platform for cross-validation. The section concludes with a performance comparison against state-of-the-art implementations.

A. Hybrid Platform Integration

Fig. 16(a) illustrates how the impedance spectroscopy PCB is integrated with a cost-effective CNC-micro-milled microfluidic device via conductive-ink electrodes, connecting through a 90-degree pin header connector instead of the conventional method of embedding gold electrodes and custom ICs directly onto a single board. This method facilitates swift prototyping and increases flexibility. A larger PCB beneath the impedance spectroscopy board houses off-chip low dropout regulators (LDOs) and FPGA connectors, acting as a central digital data communication and power distribution hub. Fig. 16(b) shows the chip micrographs for the impedance spectroscopy with a die area of $3 \times 3\ mm^2$, and Fig. 16(c) shows the luminescence detector with a die area of $1.3 \times 2\ mm^2$. Fig. 16(d) shows how the luminescence detector PCB is combined with a cost-effective CNC-micro-milled microfluidic device and interfaces with SiPMs.

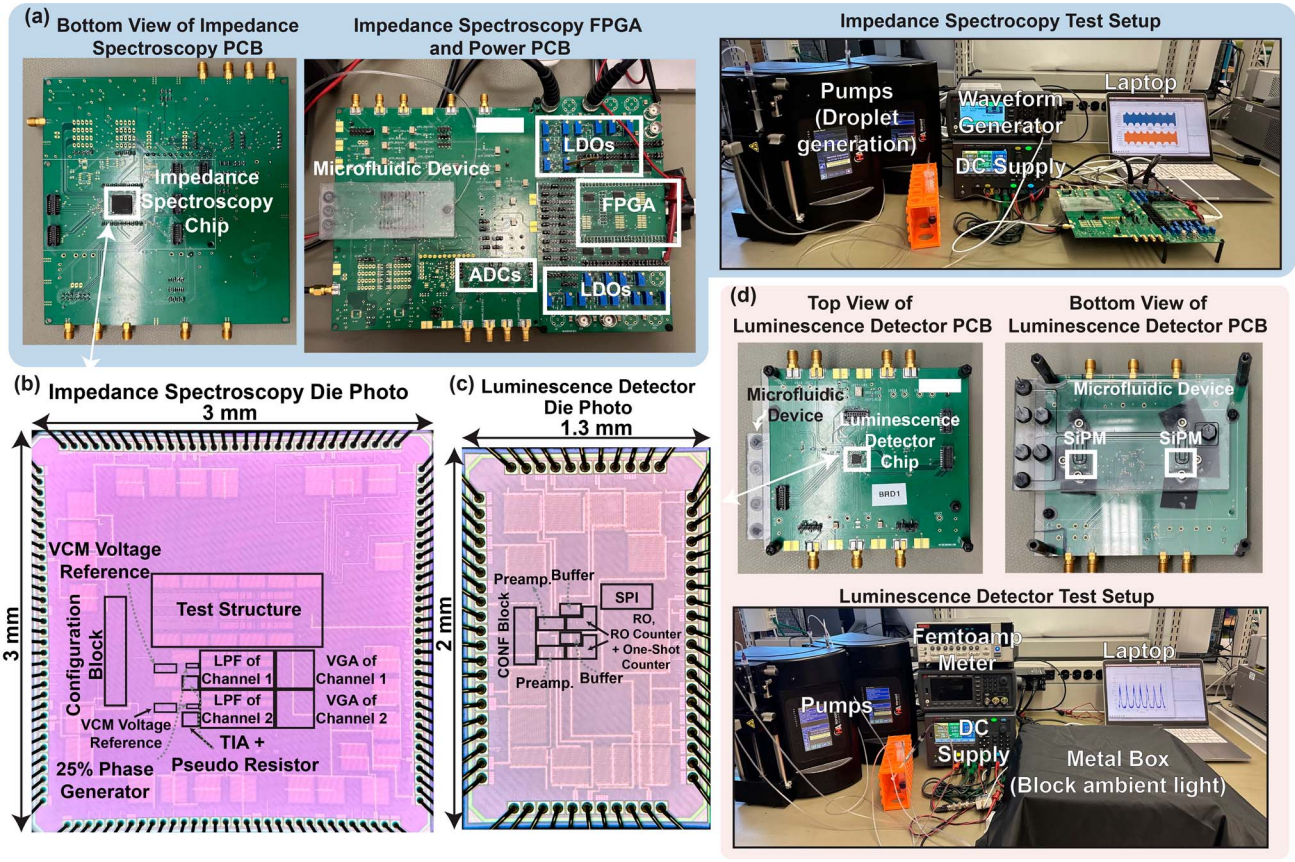

Fig. 16. (a) Impedance spectroscopy PCB top and bottom views and its measurement setup. (b) Impedance spectroscopy die photo. (c) Luminescence detector die photo. (d) Luminescence detector PCB top and bottom views and its measurement setup.

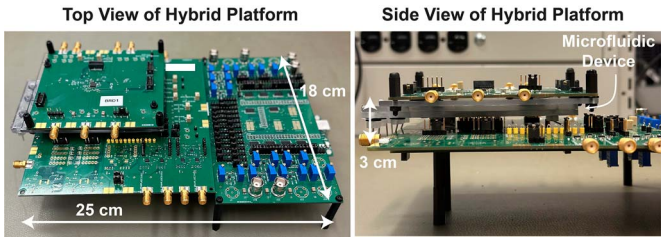

Fig. 17. Integration of the hybrid platform.

The microfluidic device embedded with the CMOS luminescence sensor also includes a light-blocking black oil to prevent cross-talk between neighboring bioluminescent droplets. Lastly, the test setups employed for impedance and luminescence measurements are shown in Fig. 16(a) and 16(d), respectively. The entire setup for the luminescence detector chip is enclosed in a metal box and wrapped with a black cloth during measurements to mitigate ambient light interference.

Fig. 17 shows the hybrid platform's top and side views. It demonstrates how the impedance spectroscopy and luminescence detector PCBs are integrated with the droplet microfluidic device. This configuration allows for the simultaneous collection of impedance and bioluminescence data from the same set of droplets, highlighting the platform's ability to gather multidimensional information at the same time.

B. Electrical Performance of the Impedance Spectroscopy

To assess the linearity and resolution of the impedance spectroscopy chip, we set up a test model consisting of a 470 $k\Omega$ resistor and a 10 pF capacitor connected in series. This model was placed between the excitation waveform generator (33622A, Keysight Technologies) and the on-chip TIA input. The test model was designed to simulate an input impedance ranging from 100 $k\Omega$ to 2 $M\Omega$.

The waveform generator was configured to produce an 802 kHz sinusoidal signal with a 600 mV DC offset. Additionally, an FPGA delivered a 50% duty cycle signal at 3.2 MHz to the on-chip phase generator's CLK input, resulting in an 800 kHz LO signal for the signal downconversion path. The capacitive element in the setup effectively removed the DC component from the excitation signal while the TIA's feedback network established the impedance model's DC node voltages. To ensure optimal linearity, the on-chip VGA was set to unity gain.

We describe the data acquisition and processing methods used for the electrical performance characterization in the relevant subsections (Sec. IV-B1 and Sec. IV-B2) before presenting the electrical performance results of the impedance spectroscopy, including linearity, resolution, and noise.

1) Data Acquisition and Processing: The impedance spectroscopy chip generates two baseband signals, I_FINAL and Q_FINAL, both at a frequency of 2 kHz, as described by Eq. 13

and Eq. 14, respectively. Here, t denotes time in seconds, and f_{IF} indicates the intermediate frequency ($|\omega_1 - \omega_2|$) of 2 kHz.

$$\text{I\_FINAL}(t) = V_I sin(2\pi f_{IF} t) \tag{13}$$

$$\text{Q\_FINAL}(t) = V_Q sin\left(2\pi f_{IF} t + \frac{\pi}{2}\right) \tag{14}$$

The amplitudes of the baseband signals, V_I for I_FINAL and V_Q for Q_FINAL, are continuously recorded by two external 16-bit, 1-MSPS analog-to-digital converters (ADCs), ADS8860, from Texas Instruments. These ADCs send the digitized information to an FPGA using the serial peripheral interface (SPI), allowing for subsequent data processing, such as curve fitting to determine V_I and V_Q. Simultaneously, I_FINAL and Q_FINAL are monitored in real-time on an oscilloscope (MSOX4154A, Keysight Technologies), which displays these signals and performs their Fast Fourier Transform (FFT) analysis. The FFT provides Root Mean Square (RMS) values, and for linearity and noise measurements, we average the FFT over 3 seconds to determine the output voltages V_I and V_Q. The oscilloscope also displays the excitation voltage $V_{exc}(\omega_1)$ and its FFT, offering a complete view of the excitation signal, which we use to estimate the input current.

The output voltage of the impedance spectroscopy chip in the following electrical characterizations is calculated as given by Eq. 15.

$$V_{IQ} = \sqrt{V_I^2 + V_Q^2} \tag{15}$$

2) Expected Input Current: We first calculate the input impedance at 802 kHz as given in Eq. 16 to calculate the expected input current for the following electrical performance measurements.

$$\begin{aligned} |Z(802\ kHz)| &= \sqrt{R_i^2 + \left(\frac{1}{2\pi f_1 C_i}\right)^2} \\ &= \sqrt{(470e3)^2 + \left(\frac{1}{2 * \pi * 802e3 * 10e-12}\right)^2} \\ &= 470.418\ k\Omega \end{aligned} \tag{16}$$

Then, the expected input current amplitude is calculated using Eq. 17.

$$I(802\ kHz) = \frac{V_{exc}(\omega_1)}{|Z(802\ kHz)|} \tag{17}$$

3) Linearity and Resolution Measurements: To measure linearity, the waveform generator increased the excitation voltage ($V_{exc}(\omega_1)$) from 2 mVpp to 94 mVpp in steps of 2 mV. Fig. 18(a) displays the 1-dB compression point, identified at an input current of 36 nA. The x-axis was derived using Eq. 17, and the y-axis using Eq. 15.

To determine the impedance spectroscopy chip's minimum resolution (i.e., its ability to detect small input current changes), we initially set the amplitude increment for the waveform generator's excitation voltage to 0.01 mVpp. We gradually increased this amplitude increment until we could reliably differentiate between two output voltages, where the output range (defined as the range of average $\pm 1\sigma$ standard deviation across 100 measurements) do not overlap between two excitation amplitudes.

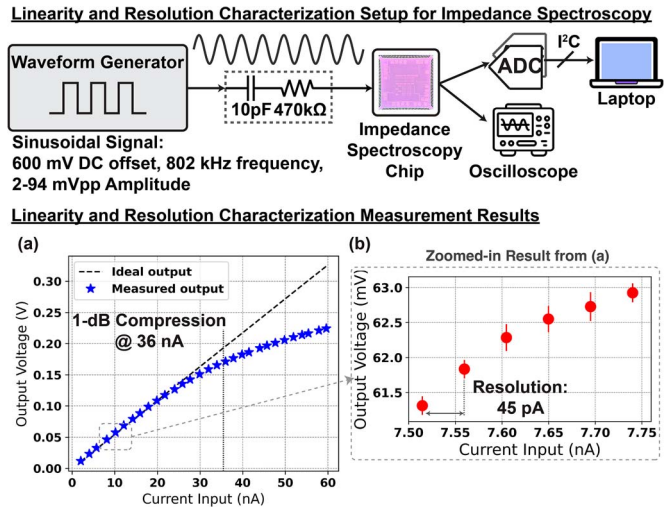

Fig. 18. Linearity and resolution performance characterization setup for the impedance spectroscopy chip, and the measurement results showing the 1-dB compression point and resolution.

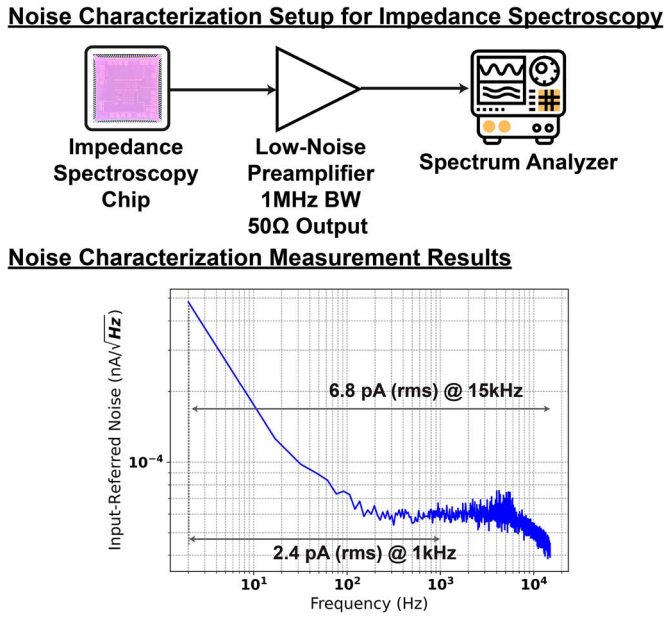

Fig. 19. Input-referred noise measurement setup and results of the impedance spectroscopy chip, showing 2.4 pA and 6.8 pA RMS at 1 kHz and 15 kHz bandwidths, respectively.

In our experiments, an increment of 0.06 mVpp was necessary to distinguish the output voltages with at least a 1σ difference, corresponding to a detectable input current difference of 45 pA, shown in Fig. 18(b).

4) Input-Referred Noise Measurement: The input-referred current noise, deduced from the output noise voltage spectrum (measured using N9030B, Keysight Technologies), was calculated by dividing through the internal gain, mainly from the TIA gain, given that the VGA was set to unity gain, and the LPF caused a negligible loss. The measurement setup used for sensitivity characterization is shown in Fig. 19. At bandwidths of 10 Hz, 1 kHz, 2 kHz, and 15 kHz, input-referred current noise

levels were measured at 1.4 pA, 2.4 pA, 3 pA, and 6.8 pA RMS, respectively. These noise level findings complement the earlier resolution metrics, showing that the impedance spectroscopy's determined resolution significantly exceeds the input-referred current noise by 6.6 times at 15 kHz.

With an input-referred current noise of 1.4 pA RMS at a bandwidth of 10 Hz and reaching the 1-dB compression point at 36 nA, the impedance sensing system demonstrates a dynamic range of 88 dB. In summary, by comparing the system's input-referred noise and linearity with those of state-of-the-art CMOS impedance spectroscopy chips, it becomes evident that it possesses the necessary precision for detecting small-volume droplets in high-throughput biosensor screening applications.

C. Real-Time Droplet Detection via Impedance Spectroscopy

All real-time droplet impedance measurements presented in the following results were obtained using the setup depicted in Fig. 18. The system operated with an excitation amplitude of 30 mVpp and a programmed pseudo-resistor value of approximately 7.6 MΩ. The system's real-time impedance spectroscopy measurements confirm its ability to detect droplets ranging from 4 to 47.9 nL in volume, moving at speeds between 67 and 1.3 mm/s, respectively. The droplets' residence times between the electrodes span milliseconds, with the shortest residence time being 3.7 ms. Droplet volume is controlled by adjusting water and oil flow rates, managed by the system's syringe pumps from Harvard Apparatus. Water is consistently pumped at a rate of 2 μL/min, denoted as Q_w, while oil flow rates vary from 2 to 50 μL/min, denoted as Q_o. Increasing the oil flow rate produces smaller droplets at higher velocities, following Eq. 18:

$$v_{droplet} = \frac{Q_w + 2 \cdot Q_o}{w_{channel} \cdot h_{channel} \cdot 60s}, \tag{18}$$

where $w_{channel}$ and $h_{channel}$ represent the width and height of the microfluidic channel's geometry, respectively.

Droplet admittance ($\Delta|Y|$) is determined by calculating the change in admittance as a droplet passes through an oil-filled channel (See Appendix for the calculation procedure). In Fig. 20(a), you can see a decrease in admittance as the droplet volume reduces due to the droplet capacitance decreasing. This observation confirms a roughly linear relationship between droplet volume and admittance/impedance, essential for future analyses linking droplet volume to admittance values.

Fig. 20(b) shows real-time droplet detection using the impedance spectroscopy chip. The I/Q outputs displayed on the oscilloscope support our findings. As seen in Fig. 20(b), the impedance spectroscopy system consistently detects aqueous droplets with volumes of 5.4, 15.4, and 32.7 nL in real-time within an oil-filled microfluidic channel, which aligns with the results from microscopy images.

D. Electrical Characterization of Luminescence Detector

Fig. 21 displays the electrical characterization of the luminescence readout chip. We used a waveform generator (33622A,

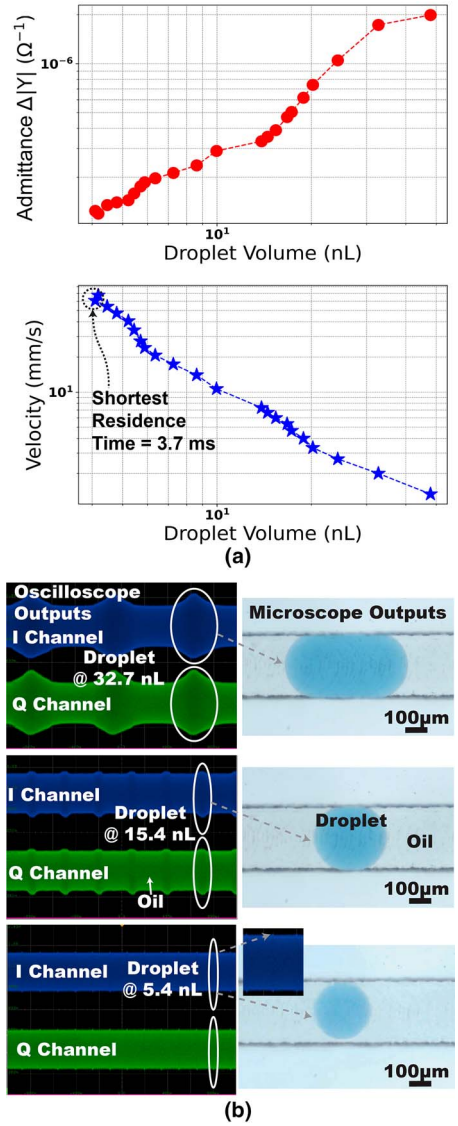

Fig. 20. Real-time droplet detection using the impedance spectroscopy chip.

Keysight Technologies) to emulate light pulses in this characterization. The pulse width was configured at 20 ns with a DC offset of 570 mV, aligning with the DC biasing parameters set for the bias-tee block. The RO-driven counter showed an increased count rate as the pulse amplitude increased, verifying its design's insensitivity to pulse frequency. In contrast, the one-shot counter was sensitive to the pulse frequency, detecting the increasing frequency of the pulses for greater amplitude, such as 16 mVpp, but reported fewer counts at a higher frequency for a target count cycle.

E. Optical Characterization of Luminescence Detector

We adjusted the supply voltage level applied to a teal LED (520 nm) to test the sensitivity of the luminescence sensor within a wide dynamic range, which resulted in SiPM photocurrents ranging from 3 nA to 20.4 μA, as measured by a sub-femtoamp source measurement instrument (K6430, Keithley

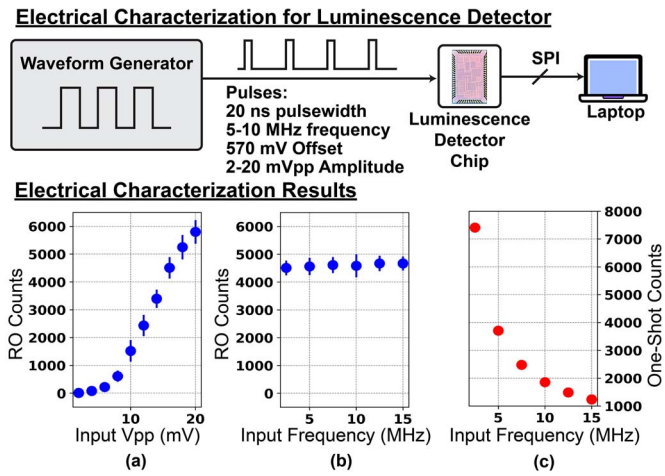

Fig. 21. Electrical characterization setup of the luminescence detector chip, including the results of varying the amplitude (a) and frequency (b) of input pulses for the on-chip Ring Oscillator (RO)-driven counter, and frequency (c) of input pulses for One-Shot counter. This measurement demonstrates the sensitivity of the RO-driven counter to light pulse amplitude variations at a Silicon Photomultiplier (SiPM) output.

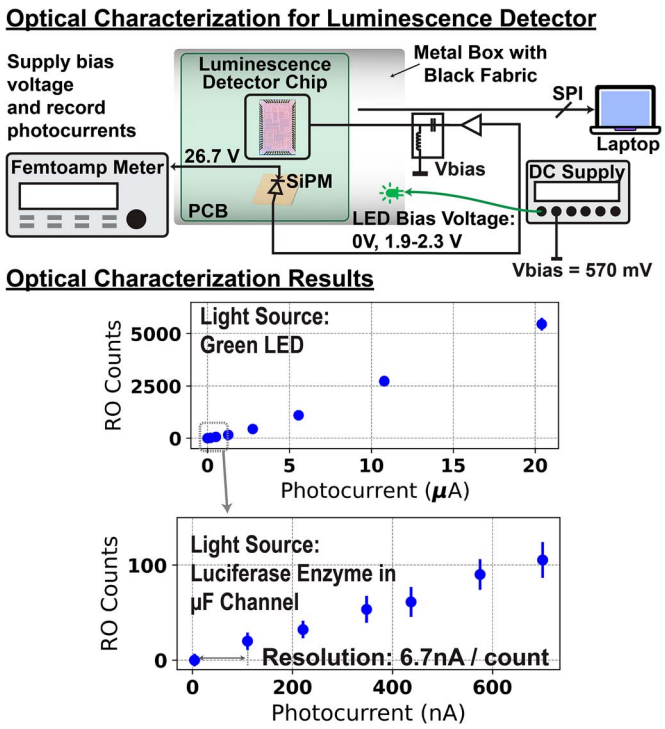

Fig. 22. Optical characterization setup and results of the luminescence detector chip with a green LED or luciferase enzyme as the light source, showing a resolution of 6.7 nA/count.

Instruments). The purpose of this method was to emulate the range of luminescence intensities detectable by the RO-driven counter. The setup for this optical characterization is illustrated in Fig. 22. We also conducted experiments within a specific luminescence range relevant to our nL-volume droplet detection application. We measured the readout at different light intensity levels emitted from a 125 nL microfluidic channel filled with

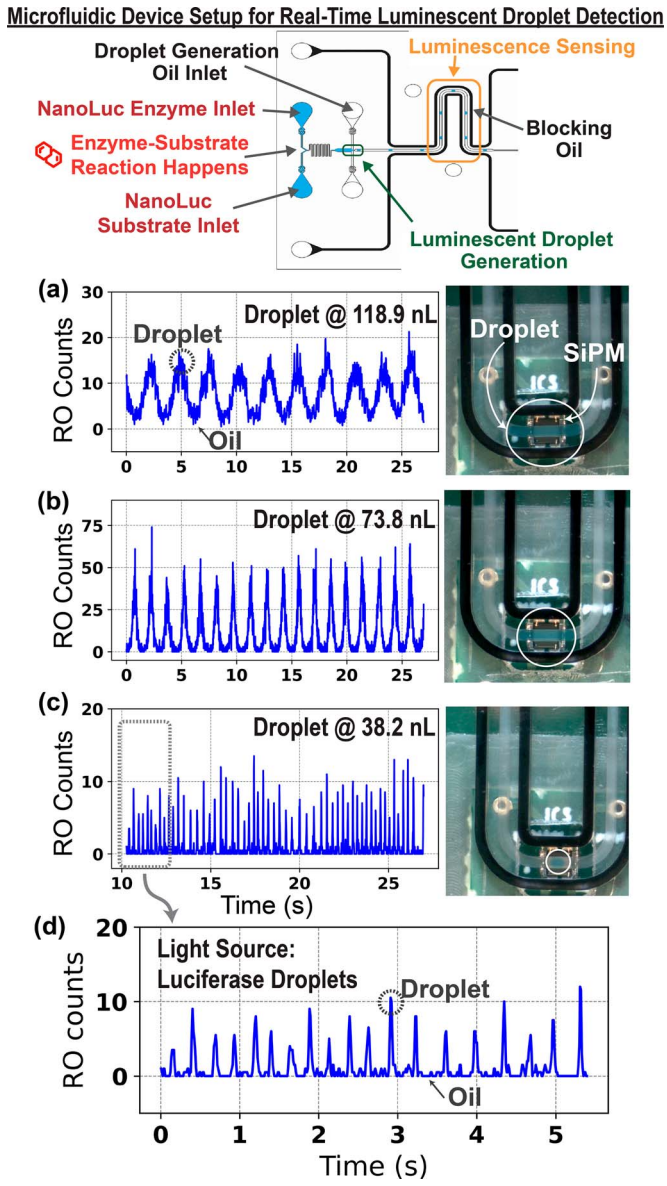

Fig. 23. Real-time sensing of 38.2-to-118.9nL luminescent droplets at velocities from 24.3-to-0.8mm/s via the luminescence detector chip, as shown in (a), (b), and (c). (d) presents a zoomed-in result of the smallest droplet volume at 38.2 nL.

NanoLuc. By adjusting the pump rates to control the mixing of the NanoLuc enzyme and substrate, we observed changes in the reaction rate (with 100 μM enzyme and a 1:50 substrate dilution), leading to different luminescence levels. The detector achieved a luminescence-sensing resolution of 6.7 nA/count. This resolution was calculated using the formula: $resolution = \frac{\Delta I_{PH}}{\Delta RO\ Count}$, where I_{PH} represents the real-time photocurrent recorded by the sub-femtoamp source measurement instrument.

F. Real-Time Sensing of NanoLuc Reaction in Droplets

All real-time droplet luminescence measurements presented in the following results were obtained using the setup shown in Fig. 22, leveraging high-resolution optical characterization

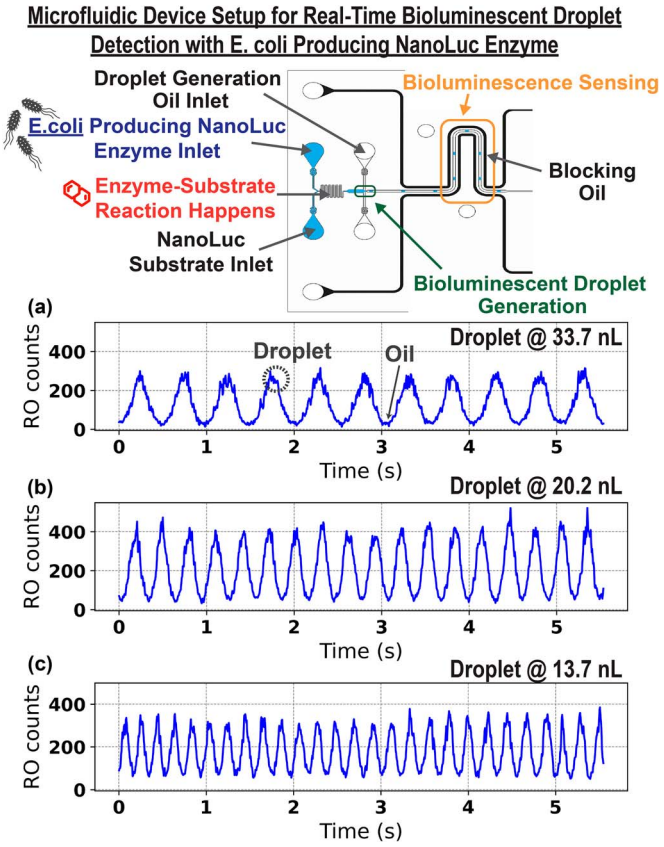

Fig. 24. Real-time detection of bioluminescent droplets using the luminescence detector chip. Bioluminescence is emitted by *E. coli* cells containing NanoLuc genetic information and producing the NanoLuc enzyme upon mixing with NanoLuc substrate at the inlet intersections. (a) to (c) show the results for droplet volumes ranging from 13.7 to 33.7 nL.

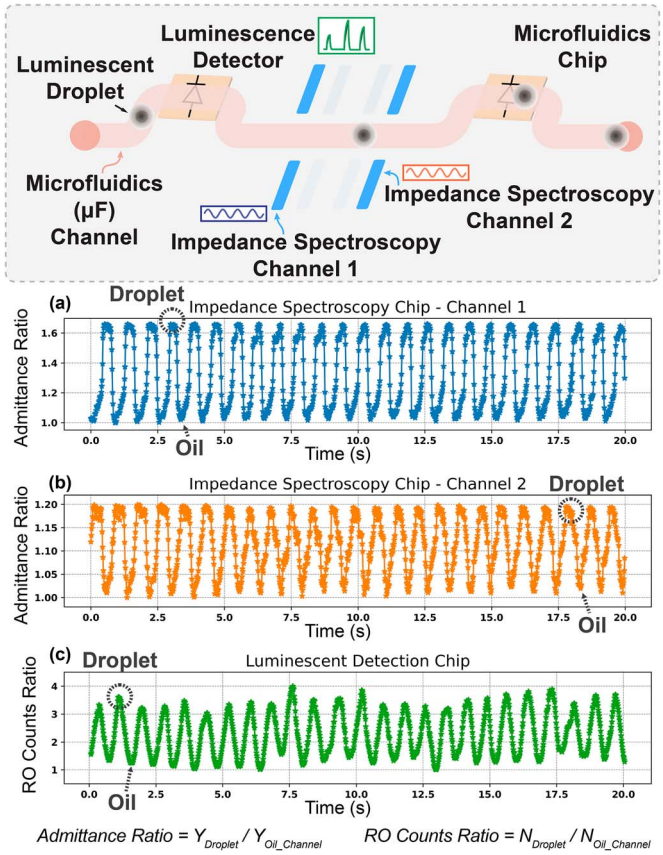

Fig. 25. Simultaneous dual-modal analysis of luminescent droplets in a microfluidic device in real-time. The setup integrates a luminescence detection chip for optical analysis and an impedance spectroscopy chip with two on-chip hardware channels for droplet impedance detection when the droplet moves through the microfluidic channel embedded with conductive-ink electrode pairs. The fully integrated system enables cross-validation of the luminescent droplet detection accuracy within the microfluidic device.

to enhance accuracy. This setup enables back-correlation between the recorded output counts and the expected photocurrent generated by the luminescent droplets. The luminescence detector effectively senses the NanoLuc luciferase enzyme-substrate reaction in real time. A 100 μM concentration of the enzyme and a 1:50 substrate dilution were used to create luminescent droplets at varying generation rates within a setup similar to the NanoLuc-filled channel. The NanoLuc enzyme and substrate were consistently infused at 2 μL/min, while the oil flow rate ranged from 2 to 90 μL/min. A different microfluidic device geometry with a wider channel width was utilized in this experiment compared to the microfluidic device presented in Section IV-C, allowing the luminescence detector chip to accurately identify luminescent droplets with volumes ranging from 38 to 119 nL, as depicted in Fig. 23. These droplets moved at a maximum velocity of 24.3 mm/s. A close-up view of the light-blocking black oil in horseshoe-shaped channels, utilized for minimizing cross-talk between the neighboring luminescent droplets, is shown in the microscopic images in Fig. 23.

G. Real-Time Sensing of Bioluminescent E. coli Droplets

The luminescence detector is capable of real-time detection of bioluminescent droplets containing *E. coli* cells modified to produce the NanoLuc enzyme. When these cells are combined with the NanoLuc substrate, they initiate a reaction that generates luciferase. Fig. 24 demonstrates that the luminescence detector chip successfully detected droplets containing *E. coli* cells and substrate at a consistent 2 μL/min delivery rate. The oil flow rate was varied between 6, 10, and 15 μL/min. This detector chip can identify bioluminescent droplets as small as 13.7 nL, with a residence time of 24.2 ms and a velocity of 4.53 mm/s. The measurement plots in Fig. 24 use a moving average of two data points to enhance detection precision, effectively reducing noise.

H. Luminescent Droplet Detection via Concurrent Dual-Modal Sensing

Fig. 25 shows concurrent measurements obtained from impedance spectroscopy and luminescence detection chips. Each channel of the impedance spectroscopy chip uses the same gain configuration as described in Section IV-C. Similarly, the threshold settings of the luminescence detector are consistent with those in Sections IV-F and IV-G. The NanoLuc enzyme and its substrates are pumped at 3 μL/min, while the oil flow rate is 5 μL/min.

TABLE I
PERFORMANCE SUMMARY AND COMPARISON WITH THE STATE-OF-THE-ART IMPEDANCE SPECTROSCOPY INTEGRATED CIRCUITS [48], [71], [72], [73], [74], [75], [76]

	This Work	TBioCAS '21 [71]	VLSI '23 [72]	CICC '18 [73]	TBioCAS '10 [48]	TBioCAS '23 [74]	BioCAS '22 [75]	LabOnChip '12 [76]
Integrated with Microfluidic?	YES	YES	YES	NO	NO	NO	YES	YES
Microfluidic Type	Continuous Flow (Droplet)	Continuous Flow (Cell / Particle)	Continuous Flow (Cell / Particle)	N.A.	N.A.	N.A.	Continuous Flow (Cell / Particle)	Digital
Modality	Impedance Spectroscopy (IS) + Luminescence Detector (LD) with SiPM	Impedance Spectroscopy (with CMOS-driven bulk flow)	Square Wave Voltcoulometry	Impedance Spectroscopy (Phase Detector)	Impedance Spectroscopy	Electrochemical + Optical Shadow Imaging + Impedance Sensing	Electrophysiology (Ele-phy) + Impedance Sensing (IS)	AM-EWOD Device with Impedance Sensing for Close-Loop Droplet Control [+]
Droplet Volume (nL)	4 - 47.9 (IS) 38.2 - 118.9 (LD)	N.A.	N.A.	N.A.	N.A.	N.A.	N.A.	5 - 550
Electrode	Conductive Ink	Gold	On-Chip Gold	On-Chip Gold	On-Chip Gold	On-Chip Titanium/Gold/Silver	On-Chip Platinum	Hydrophobic Indium Tin Oxide
Technology (nm)	65nm CMOS	65nm CMOS	180nm CMOS	180nm CMOS	350nm CMOS	130nm BiCMOS	180nm CMOS	Thin Film Transistor
Supply Voltage (V)	1.2	1.2	1.8	1.8	3.3	1.2	1.8	N.R.
Excitation Frequency (kHz)	400 - 1000	N.R.	N.R.	5 - 1000	0.01 - 50000	N.A.	0.001 - 1000	N.A.
Max Velocity (mm/s)	67 (IS) 24 (LD)	0.16	N.R.	N.A.	N.A.	N.A.	N.R.	N.A.
Transimpedance Gain (MΩ)	24.4 (IS)	0.10	1.00	N.A.	0.01	N.A.	N.A.	N.A.
Preamplifier Gain (dB)	28 (LD) [++]	N.A.	N.A.	N.A.	N.A.	N.A.	29 – 76 (Ele-phy)	N.A.
Power Consumption (μW)	318 (IS) 598 (LD)	250 *	2400 **	197 *	720 ***	3000***	24 (Ele-phy) 385 (IS)	N.R.
Resolution	45 pA (IS) 6.7 nA / count (LD)	N.R.	N.R.	N.R.	330 pA [#] (IS)	2 pA	N.R.	N.R.
Input-Referred Noise (pA_{rms}) @ 1kHz	2.4 (IS)	812	18.1 / 5.2 [##]	N.R.	577	N.R.	N.R.	N.A.
Dynamic Range	88 dB [&] (IS)	95 dB [&]	N.A.	N.A.	97 dB [&]	90 dB [&&]	N.R.	1.3 V [&&&]

[+] Active Matrix Electrowetting on Dielectric (AM-EWOD)
[++] Post-layout simulated preamplifier gain
* Power consumption per channel
** Heater not included
*** Per pixel group
[#] Current sensitivity at BW = 10Hz
[##] IRN using square waveform voltammetry and square wave voltcoulometry
[&] Reported for 10Hz bandwidth
[&&] Calculated using reported Imax and sensitivity
[&&&] Difference of typical sensor output signal swing between droplet present and absent
N.A. = Not applicable N.R. = Not reported

The y-axes of the first two subplots display the admittance ratios between the luminescent droplets and the oil channel derived from the ADC outputs reading real-time I/Q values. Variations in admittance ratios between channels one and two are due to fabrication disparities among different conductive ink electrode pairs. Pre-measurement calibration for each electrode pair could reduce these variations in future impedance measurements. The y-axis of the third subplot illustrates the RO counter output ratio, differentiating luminescent droplets from the oil channel. Lower ratio values indicate the presence of oil, while higher values with peaks suggest droplet detection.

In this simultaneous measurement, both methods identified 25 droplets within a 20-second time frame. The corroborative data from these separate chips indicate that the two modalities can be used to mutually validate results. This validation is critical to ensure that impedance and luminescence sensing accurately capture all droplets. Relying solely on luminescence detection is insufficient for reliably determining droplet counts without the complementary use of impedance sensing. By validating both modalities, we establish confidence in the data from both methods, enabling future work to correlate droplet impedance values with bioluminescent cell density.

I. Performance Summary and Comparison

Table I summarizes the system's performance metrics and compares them with the current state-of-the-art impedance sensing in CMOS ICs [48], [71], [72], [73], [74], [75], [76]. This project combines custom-designed CMOS ICs and cost-effective droplet microfluidics, representing the first proof-of-concept demonstration, to the best of the authors' knowledge, of impedance spectroscopy paired with luminescence sensing for high-throughput screening of bioluminescent droplets with nL volume. Concerning power efficiency, the system matches the latest advancements, consuming 318 μW for impedance spectroscopy and 598 μW for the luminescence detector from a 1.2 V supply. Notably, the input-referred noise at 1 kHz is 2.2$\times$ lower than that reported in [72], demonstrating significant advancements in sensitivity. One of the main objectives of this work is to replace bulky desktop instruments for impedance and luminescence measurements in droplet microfluidic platforms with compact, custom-designed CMOS ICs. Therefore, we compared our droplet detection accuracy with LCR and sub-femtoamp meters. While commercial equipment offers higher readout resolution, it is not optimized for droplet detection and is constrained by slower sampling rates due to communication delays with data acquisition systems. Such equipment struggles to accurately identify droplets moving at higher speeds. This issue arises because the droplet's residence time may be shorter than the sampling period. Consequently, commercial equipment can lead to omissions in the measurement data. Hence, using commercial equipment could result in missed droplet detection at high throughput, as demonstrated in Fig. 26.

By incorporating custom ICs, we significantly improved the sampling rate using our real-time sensor front end and implemented a serial communication protocol within an FPGA to reduce delays. As depicted in Fig. 26, our system achieved

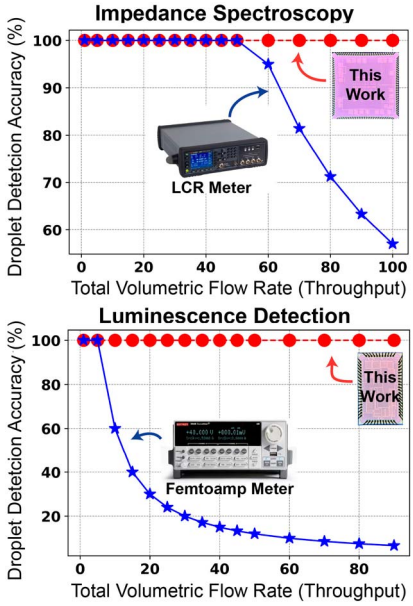

Fig. 26. Comparison with commercial solutions for impedance spectroscopy and luminescence sensing in a droplet microfluidic platform.

100% droplet detection coverage across the range of droplet velocities presented in Sections IV-C, IV-F, and IV-G. The droplet detection coverage is defined by Eq. 19, with t_r specified in Eq. 2. The sampling period is influenced by the data communication latency between the device and the laptop used for data collection.

$$Droplet\ Detection\ Coverage\ (\%) = \frac{100 \cdot t_r}{Sampling\ Period} \tag{19}$$

For future integration and miniaturization, the external waveform generator in the impedance spectroscopy architecture could be replaced with an on-chip excitation generator using an FPGA clock signal, followed by low-pass and high-pass filtering, and attenuation to drive the off-chip electrode pair, as demonstrated in [71].

V. Conclusion

This work advances the integration of high-throughput droplet microfluidics with CMOS integrated circuits for synthetic biology applications. Our hybrid platform combines high-resolution and low-noise CMOS impedance spectroscopy with sensitive luminescence detection, enabling rapid biosensor screening and optimization. The key innovation lies in the first demonstration of co-designed, low-cost, modular droplet microfluidic devices and CMOS sensors enabling real-time detection and analysis of nanoliter bioluminescent droplets. Specifically, our impedance spectroscopy chip can accurately differentiate droplet sizes from 4 to 47.9 nL at a velocity ranging from 67 to 1.3 mm/s, while the luminescence detector chip achieves precise real-time measurements of bioluminescent droplets with a resolution of 6.7 nA/count. This integration significantly improves traditional biosensor testing by eliminating labor-intensive protocols, thus enhancing the system's modularity, adaptability, and cost-effectiveness.

Appendix
Admittance Calculation for Real-Time Droplet Detection via Impedance Spectroscopy

We calculated the droplet admittance using ADC readouts for our real-time droplet detection experiments. We chose this method instead of FFT values because data transfer from the ADCs to the laptop is quicker than from the oscilloscope. Throughout these measurements, we set the excitation voltage to 35 mVpp at 802 kHz.

In each experiment to determine droplet volumes, we performed a minimum of 100 read-and-write operations to the First-In, First-Out (FIFO) buffer using the SPI to interface with the ADCs. We increased the number of operations for experiments involving larger volume droplets to capture extended residence times accurately. During each operation on the FPGA, we collected 8192 data samples from each ADC for the I_FINAL and Q_FINAL signals, totaling 16,384 samples. To reconstruct an entire 2 kHz period, approximately 147 ADC readouts are required. For data analysis, we divided the data into 147-point blocks and applied sine wave curve fitting to determine the amplitudes of the I_FINAL and Q_FINAL signals.

After calculating the amplitudes of each data segment for the I/Q baseband signals (V_I and V_Q), we computed the output voltage V_{IQ} as outlined in Eq. 15. The V_{IQ} values were then organized in ascending order, with lower amplitudes indicating oil and higher amplitudes indicating water droplets. We determined the differential output voltage $\Delta|V_{IQ}|$ for each droplet size by computing the difference between the lowest 100 V_{IQ} values and the highest 100 V_{IQ} values.

Similar to the FFT approach discussed in Section IV-B1, we can calculate the input admittance as given by Eq. 20.

$$\begin{aligned} \Delta|Y| &= \frac{1}{\Delta|Z|} = \frac{1}{|Z_w - Z_o|} \\ \Delta|Z| &= \frac{A_{TIA} \cdot A_{LPF} \cdot A_{VGA} \cdot |V_{exc}(\omega_1)|}{\Delta|V_{IQ}|}. \end{aligned} \tag{20}$$

Acknowledgment

The authors would like to thank Phillip Nadeau, Arslan Riaz, Chengjie Zhu, and David McIntyre for technical discussions, Jingyao Chen for providing the *E. coli* cells, and the Boston University Biological Design Center for supporting the synthetic biology research infrastructure.

References

[1] M. Mimee et al., "An ingestible bacterial-electronic system to monitor gastrointestinal health," *Science*, vol. 360, no. 6391, pp. 915–918, 2018.
[2] M. E. Inda-Webb et al., "Sub-1.4 cm3 capsule for detecting labile inflammatory biomarkers *in situ*," *Nature*, vol. 620, no. 7973, pp. 386–392, 2023.
[3] L. G. Olias and M. Di Lorenzo, "Microbial fuel cells for in-field water quality monitoring," *RSC Adv.*, vol. 11, no. 27, pp. 16307–16317, 2021.

[4] S. Sevda et al., "Biosensing capabilities of bioelectrochemical systems towards sustainable water streams: Technological implications and future prospects," *J. Biosci. Bioeng.*, vol. 129, no. 6, pp. 647–656, 2020.

[5] J. Shi, D. Feng, and Y. Li, "Biosensors in fermentation applications," in *Fermentation Processes*, Rijeka, Croatia: IntechOpen, 2017.

[6] Y. Ye, H. Guo, and X. Sun, "Recent progress on cell-based biosensors for analysis of food safety and quality control," *Biosensors Bioelectron.*, vol. 126, pp. 389–404, Feb. 2019.

[7] N. Gupta, V. Renugopalakrishnan, D. Liepmann, R. Paulmurugan, and B. D. Malhotra, "Cell-based biosensors: Recent trends, challenges and future perspectives," *Biosensors Bioelectron*, vol. 141, Sep. 2019, Art. no. 111435.

[8] J. A. Kaczmarek and K. L. J. Prather, "Effective use of biosensors for high-throughput library screening for metabolite production," *J. Ind. Microbiol. Biotechnol.*, vol. 48, nos. 9–10, 2021, Art. no. 49.

[9] F. Cheng, X. L. Tang, and T. Kardashliev, "Transcription factor-based biosensors in high-throughput screening: Advances and applications," *Biotechnol. J.*, vol. 13, no. 7, 2018, Art. no. 1700648.

[10] P. Hanson-Manful and W. M. Patrick, "Construction and analysis of randomized protein-encoding libraries using error-prone PCR," *Methods Mol. Biol.*, vol. 996, pp. 251–267, Feb. 2013.

[11] P. C. Gach, K. Iwai, P. W. Kim, N. J. Hillson, and A. K. Singh, "Droplet microfluidics for synthetic biology," *Lab Chip*, vol. 17, no. 20, pp. 3388–3400, Oct. 2017.

[12] G. Luka et al., "Microfluidics integrated biosensors: A leading technology towards lab-on-a-chip and sensing applications," *Sensors*, vol. 15, no. 12, 2015, Art. no. 30011.

[13] T. Moragues et al., "Droplet-based microfluidics," *Nature Rev. Methods Primers* 2023 3:1, vol. 3, no. 1, pp. 1–22, Apr. 2023.

[14] J. J. Agresti et al., "Ultrahigh-throughput screening in drop-based microfluidics for directed evolution," *Proc. Nat. Acad. Sci. US A*, vol. 107, no. 9, pp. 4004–4009, 2010.

[15] M. T. Guo, A. Rotem, J. A. Heyman, and D. A. Weitz, "Droplet microfluidics for high-throughput biological assays," *Lab Chip*, vol. 12, no. 12, pp. 2146–2155, 2012.

[16] A. B. Theberge, G. Whyte, and W. T. S. Huck, "Generation of picoliter droplets with defined contents and concentration gradients from the separation of chemical mixtures," *Anal. Chem.*, vol. 82, no. 9, pp. 3449–3453, 2010.

[17] A. Sarnaik, A. Liu, D. Nielsen, and A. M. Varman, "High-throughput screening for efficient microbial biotechnology," *Curr. Opin. Biotechnol.*, vol. 64, pp. 141–150, Aug. 2020.

[18] D. Koveal et al., "A high-throughput multiparameter screen for accelerated development and optimization of soluble genetically encoded fluorescent biosensors," *Nature Commun.*, vol. 13, no. 1, pp. 1–14, 2022.

[19] T. Axelrod, E. Eltzov, and R. S. Marks, "Bioluminescent bioreporter pad biosensor for monitoring water toxicity," *Talanta*, vol. 149, pp. 290–297, Mar. 2016.

[20] E. Eltzov, A. Cohen, and R. S. Marks, "Bioluminescent liquid light guide pad biosensor for indoor air toxicity monitoring," *Anal. Chem.*, vol. 87, pp. 3655–3661, Apr. 2015.

[21] L. Cevenini et al., "A novel bioluminescent nanoluc yeast-estrogen screen biosensor (nanoyes) with a compact wireless camera for effect-based detection of endocrine-disrupting chemicals," *Anal. Bioanal. Chem.*, vol. 410, pp. 1237–1246, Feb. 2018.

[22] Q. Liu et al., "A threshold-based bioluminescence detector with a CMOS-integrated photodiode array in 65 nm for a multi-diagnostic ingestible capsule," *IEEE J. Solid-State Circuits*, vol. 58, no. 3, pp. 838–851, Mar. 2023.

[23] Q. Liu et al., "17.7 droplet microfluidics co-designed with real-time CMOS luminescence sensing and impedance spectroscopy. 4nL droplets at a 67mm/s velocity," *Dig. Tech. Papers - IEEE Int. Solid-State Circuits Conf.*, pp. 326–328, 2024.

[24] S. M. Scott and Z. Ali, "Fabrication methods for microfluidic devices: An overview," *Micromachines*, vol. 12, no. 3, 2021, Art. no. 319.

[25] B. K. Gale et al., "A review of current methods in microfluidic device fabrication and future commercialization prospects," *Inventions*, vol. 3, no. 3, 2018.

[26] A. G. Niculescu, C. Chircov, A. C. Bîrcă, and A. M. Grumezescu, "Fabrication and applications of microfluidic devices: A review," *Int. J. Mol. Sci.*, vol. 22, no. 4, pp. 1–26, 2021.

[27] H. Klank, J. P. Kutter, and O. Geschke, "CO(2)-laser micromachining and back-end processing for rapid production of PMMA-based microfluidic systems," *Lab Chip*, vol. 2, no. 4, pp. 242–246, Nov. 2002.

[28] J. Y. Cheng, C. W. Wei, K. H. Hsu, and T. H. Young, "Direct-write laser micromachining and universal surface modification of PMMA for device development," *Sensors Actuators B-Chem.*, vol. 99, no. 1, pp. 186–196, 2004.

[29] N. C. Nayak, Y. C. Lam, C. Y. Yue, and A. T. Sinha, "CO2-laser micromachining of PMMA: The effect of polymer molecular weight," *J. Micromechanics Microeng.*, vol. 18, no. 9, 2008, Art. no. 095020.

[30] N. Bhattacharjee, A. Urrios, S. Kang, and A. Folch, "The upcoming 3D-printing revolution in microfluidics," *Lab Chip*, vol. 16, no. 10, pp. 1720–1742, 2016.

[31] S. Waheed et al., "3D printed microfluidic devices: Enablers and barriers," *Lab Chip*, vol. 16, no. 11, pp. 1993–2013, 2016.

[32] A. V. Nielsen, M. J. Beauchamp, G. P. Nordin, and A. T. Woolley, "3D printed microfluidics," *Annu. Rev. Anal. Chem.*, vol. 13, pp. 45–65, Jun. 2020.

[33] D. J. Guckenberger, T. E. De Groot, A. M. Wan, D. J. Beebe, and E. W. Young, "Micromilling: A method for ultra-rapid prototyping of plastic microfluidic devices," *Lab Chip*, vol. 15, no. 11, pp. 2364–2378, Jun. 2015.

[34] P. Nath et al., "Polymerase chain reaction compatibility of adhesive transfer tape based microfluidic platforms," *Microsyst. Technol.*, vol. 20, no. 6, pp. 1187–1193, 2014.

[35] J. M. Zhang, Q. Ji, and H. Duan, "Three-dimensional printed devices in droplet microfluidics," *Micromachines*, vol. 10, no. 11, 2019, Art. no. 754, doi: https://doi.org/10.3390/mi10110754.

[36] A. K. Au, W. Huynh, L. F. Horowitz, and A. Folch, "3D-printed microfluidics," *Angewandte Chemie Int. Ed.*, vol. 55, no. 12, pp. 3862–3881, 2016.

[37] A. Lashkaripour, R. Silva, and D. Densmore, "Desktop micromilled microfluidics," *Microfluidics Nanofluidics*, vol. 22, no. 3, pp. 1–13, 2018.

[38] B. S. Yilbas et al., "Wetting and other physical characteristics of polycarbonate surface textured using laser ablation," *Appl. Surf. Sci.*, vol. 320, pp. 21–29, Nov. 2014.

[39] J. C. Baret, "Surfactants in droplet-based microfluidics," *Lab Chip*, vol. 12, no. 3, pp. 422–433, 2012.

[40] J. C. Baret et al., "Fluorescence-activated droplet sorting (FADS): Efficient microfluidic cell sorting based on enzymatic activity," *Lab Chip*, vol. 9, no. 13, pp. 1850–1858, Jul. 2009.

[41] H. E. Ayliffe, A. B. Frazier, and R. D. Rabbitt, "Electric impedance spectroscopy using microchannels with integrated metal electrodes," *IEEE J. Microelectromech. Syst.*, vol. 8, no. 1, pp. 50–56, Mar. 1999.

[42] D. McIntyre, A. Lashkaripour, and D. Densmore, "Rapid and inexpensive microfluidic electrode integration with conductive ink," *Lab a Chip*, vol. 20, no. 20, pp. 3690–3695, 2020.

[43] C. Priest, S. Herminghaus, and R. Seemann, "Controlled electrocoalescence in microfluidics: Targeting a single lamella," *Appl. Phys. Lett.*, vol. 89, no. 13, 2006, Art. no. 134101.

[44] A. Sciambi and A. R. Abate, "Generating electric fields in PDMS microfluidic devices with salt water electrodes," *Lab Chip*, vol. 14, no. 15, pp. 2605–2609, 2014.

[45] A. Lashkaripour et al., "Machine learning enables design automation of microfluidic flow-focusing droplet generation," *Nature Commun.*, vol. 12, Dec. 2021, Art. no. 25.

[46] S. Michaelis, J. Wegener, and R. Robelek, "Label-free monitoring of cell-based assays: Combining impedance analysis with SPR for multiparametric cell profiling," *Biosensors Bioelectron.*, vol. 49, pp. 63–70, Nov. 2013.

[47] M. Seok, G. Kim, D. Blaauw, and D. Sylvester, "A portable 2-transistor picowatt temperature-compensated voltage reference operating at 0.5 v," *IEEE J. Solid-State Circuits*, vol. 47, no. 10, pp. 2534–2545, Oct. 2012.

[48] A. Manickam, A. Chevalier, M. McDermott, A. D. Ellington, and A. Hassibi, "A CMOS electrochemical impedance spectroscopy (EIS) biosensor array," *IEEE Trans. Biomed. Circuits Syst.*, vol. 4, no. 6 PART 1, pp. 379–390, Dec. 2010.

[49] D. Djekic, G. Fantner, K. Lips, M. Ortmanns, and J. Anders, "A 0.1% THD, 1-MΩ to 1-GΩ tunable, temperature-compensated transimpedance amplifier using a multi-element pseudo-resistor," *IEEE J. Solid-State Circuits*, vol. 53, no. 7, pp. 1913–1923, Jul. 2018.

[50] A. Tajalli, Y. Leblebici, and E. J. Brauer, "Implementing ultra-high-value floating tunable CMOS resistors," *IEEE Electron. Lett.*, vol. 44, no. 5, pp. 349–350, Feb. 2008.

[51] B. D. Padullaparthi, "Appendix J: Photodetectors," in *VCSEL Industry*. Hoboken, NJ, USA: Wiley, Nov. 2021, pp. 297–309.

[52] F. Acerbi and S. Gundacker, "Understanding and simulating SiPMs," *Nuclear Instruments and Methods in Physics Research Section A: Accelerators, Spectrometers, Detectors and Associated Equipment*, vol. 926, pp. 16–35, May 2019.

[53] A. Muntean et al., "Blumino: The first fully integrated analog SiPM with on-chip time conversion," *IEEE Trans. Radiat. Plasma Med. Sciences*, vol. 5, no. 5, pp. 671–678, Sep. 2021.
[54] Q. Lin et al., "A 119dB dynamic range charge counting light-to-digital converter for wearable PPG/NIRS monitoring applications," *IEEE Trans. Biomed. Circuits Syst.*, vol. 14, no. 4, pp. 800–810, Aug. 2020.
[55] F. Acerbi, G. Paternoster, A. Gola, V. Regazzoni, N. Zorzi, and C. Piemonte, "High-density silicon photomultipliers: Performance and linearity evaluation for high efficiency and dynamic-range applications," *IEEE J. Quantum Electron.*, vol. 54, no. 2, Apr. 2018.
[56] R. Agishev et al., "Lidar with SiPM: Some capabilities and limitations in real environment," *Opt. & Laser Technol.*, vol. 49, pp. 86–90, Jul. 2013.
[57] S. Saha, Y. Lu, F. Lesage, and M. Sawan, "Wearable SiPM-based NIRS interface integrated with pulsed laser source," *IEEE Trans. Biomed. Circuits Syst.*, 2019, vol. 13, no. 6, pp. 1313–1323, Dec. 2019.
[58] R. Re et al., "Probe-hosted silicon photomultipliers for time-domain functional near-infrared spectroscopy: phantom and *in vivo* tests," *Neurophotonics*, vol. 3, no. 4, 2016, Art. no. 045004.
[59] M. Mazzillo et al., "Noise reduction in silicon photomultipliers for use in functional near-infrared spectroscopy," *IEEE Trans. Radiat. Plasma Med. Sci.*, vol. 1, no. 3, pp. 212–220, May 2017.
[60] M. F. Santangelo, E. L. Sciuto, A. C. Busacca, S. Petralia, S. Conoci, and S. Libertino, "SiPM as miniaturised optical biosensor for DNA-microarray applications," *Sens. Bio-Sens. Res.*, vol. 6, pp. 95–98, Dec. 2015.
[61] M. Caccia, L. Nardo, R. Santoro, and D. Schaffhauser, "Silicon photomultipliers and SPAD imagers in biophotonics: Advances and perspectives," *Nucl. Instruments Methods Phys. Res. Sect. A: Accelerators, Spectrometers, Detectors Associated Equip.*, vol. 926, pp. 101–117, May 2019.
[62] D. Kalashnikov and L. A. Krivitsky, "Measurement of photon correlations with multipixel photon counters," *J. Opt. Soc. America B*, vol. 31, no. 10, Jul. 2014, Art. no. B25.
[63] K. A. Balygin, V. I. Zaitsev, A. N. Klimov, S. P. Kulik, and S. N. Molotkov, "A quantum random number generator based on the 100-Mbit/s poisson photocount statistics," *J. Exp. Theor. Phys.*, vol. 126, no. 6, pp. 728–740, 2018.
[64] X. Yang et al., "A bio-inspired spiking vision chip based on SPAD imaging and direct spike computing for versatile edge vision," *IEEE J. Solid-State Circuits*, vol. 59, no. 6, pp. 1883–1898, Jun. 2024.
[65] T. Talala, E. Parkkinen, and I. Nissinen, "CMOS SPAD line sensor with fine-tunable parallel connected time-to-digital converters for raman spectroscopy," *IEEE J. Solid-State Circuits*, vol. 58, no. 5, pp. 1350–1361, May 2023.
[66] S. Seifert, G. Van Der Lei, H. T. Van Dam, and D. R. Schaart, "First characterization of a digital SiPM based time-of-flight PET detector with 1 mm spatial resolution," *Phys. in Med. & Biol.*, vol. 58, no. 9, Apr. 2013, Art. no. 3061.
[67] Q. Lin et al., "A 196μW, reconfigurable light-to-digital converter with 119dB dynamic range, for wearable PPG/NIRS sensors," in *Proc. IEEE Symp. VLSI Circuits, Dig. Tech. Papers*, 2019, pp. C58–C59.
[68] S. Seifert et al., "Simulation of silicon photomultiplier signals," *IEEE Trans. Nucl. Sci.*, vol. 56, no. 6, pp. 3726–3733, Dec. 2009.
[69] E. Conca et al., "Large-Area, Fast-gated digital SiPM with integrated TDC for portable and wearable time-domain NIRS," *IEEE J. Solid-State Circuits*, vol. 55, no. 11, pp. 3097–3111, Nov. 2020.
[70] M. Perenzoni, D. Perenzoni, and D. Stoppa, "A 64 $\times$ 64-pixels digital silicon photomultiplier direct TOF sensor with 100-MPhotons/s/pixel background rejection and imaging/altimeter mode with 0.14% precision up to 6 km for spacecraft navigation and landing," *IEEE J. Solid-State Circuits*, vol. 52, no. 1, pp. 151–160, Jan. 2017.
[71] C. Zhu, J. Maldonado, and K. Sengupta, "CMOS-based electrokinetic microfluidics with multi-modal cellular and bio-molecular sensing for end-to-end point-of-care system," *IEEE Trans. Biomed. Circuits Syst.*, vol. 15, no. 6, pp. 1250–1267, Dec. 2021.
[72] Y.-T. Hsiao et al., "C8-5 A CMOS/microfluidics point-of-care SoC employing square-wave voltcoulometry for biosensing with aptamers and CRISPR-Cas12a enzymes," in *Proc. IEEE Symp. VLSI Technol. Circuits (VLSI Technol. Circuits)*, 2023, pp. 1–2.
[73] C. L. Hsu, A. Sun, Y. Zhao, E. Aronoff-Spencer, and D. A. Hall, "A 16 $\times$ 20 electrochemical CMOS biosensor array with in-pixel averaging using polar modulation," in *Proc. IEEE Custom Integr. Circuits Conf. (CICC),* 2018, pp. 1–4.
[74] D. Lee et al., "A multi-functional CMOS biosensor array with on-chip DEP-assisted sensing for rapid low-concentration analyte detection and close-loop particle manipulation with no external electrodes," *IEEE Trans. Biomed. Circuits Syst.*, vol. 17, no. 6, pp. 1214–1226, Dec. 2023.
[75] R. Bounik, J. Lee, V. Viswam, F. Cardes, M. M. Modena, and A. Hierlemann, "A CMOS microelectrode array integrated into an open, continuously perfused microfluidic system," in *Proc. - IEEE Biomed. Circuits Syst. Conf.: Intell. Biomed. Syst. a Better Future, Proc.*, 2022, pp. 491–494.
[76] B. Hadwen et al., "Programmable large area digital microfluidic array with integrated droplet sensing for bioassays," *Lab Chip*, vol. 12, no. 18, pp. 3305–3313, Sep. 2012.

Qijun Liu (Student Member, IEEE) received the B.Sc. degree in electrical and computer systems engineering from Rensselaer Polytechnic Institute, Troy, in 2016, and the Ph.D. degree in electrical engineering from Boston University, in 2024. She specializes in ultra-low-power mixed-signal circuit design for biomedical applications. Her research has been presented at the 2021 IEEE Custom Integrated Circuits Conference (CICC) and the International Solid-State Circuits Conference (ISSCC) Student Research Preview in 2021 and 2024, and published in the *Journal of Solid-State Circuits* (JSSC) and *Nature*. She was awarded first place in the 2019 International Microwave Symposium (IMS) and Radio Frequency Integrated Circuits Symposium (RFIC) Graduate Student Challenge. Additionally, she has been honored with the ISSCC 2020 Student Travel Grant, the ISSCC 2023 Predoctoral Achievement Award, the ISSCC 2024 Rising Star Award, and the Boston University 2024 Outstanding Electrical Engineering Dissertation Award.

Diana Arguijo Mendoza (Student Member, IEEE) received the B.Sc. degree in biomedical engineering and electrical and computer engineering from Duke University, Durham, NC. She is currently working toward the Ph.D degree with the Department of Biomedical Engineering, Boston University, Boston, MA, USA. Since 2020, she has been a member of the CIDAR Laboratory, Boston University. Her research interests include droplet microfluidic automation for synthetic biology applications.

Alperen Yasar (Student Member, IEEE) received the B.Sc. degree in electronics engineering from Sabanci University, Istanbul, Turkey, in 2021. He is currently working toward the Ph.D. degree with the Department of Electrical and Computer Engineering, Boston University, Boston, MA, USA. Since 2021, he has been a member of the Wireless Integrated Systems and Extreme Circuits Laboratory, Boston University. His research interests focus on ultralow-power analog design for biomedical applications and analog/RF solutions for physical-layer security.

Dilara Caygara (Student Member, IEEE) received the B.S. degree with a double major in electrical and electronics engineering and physics from the Middle East Technical University. She is currently working toward the Ph.D. degree with Boston University, joining the Wireless Integrated and Extreme (WISE) Circuits Laboratory under the guidance of Professor Rabia Tugce Yazicigil. Additionally, she is co-advised by Professor Douglas Densmore. Her research focuses on developing fully-integrated hardware solutions for highly efficient and scalable biosensing applications, particularly in environmental monitoring and wastewater surveillance. She is also involved in automating the co-design of microfluidic-electronic integrated systems for these applications.

Aya Kassem is currently working toward the B.S. degree in computer engineering with a concentration in machine learning with Boston University. She is currently a Research Assistant with CIDAR Lab where she focuses on the fabrication and electronics integration of microfluidic chips.

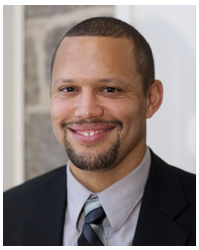

Douglas Densmore (Senior Member, IEEE) is the Tegan Family Distinguished Faculty Fellow, a Kern Faculty Fellow, a Hariri Institute for Computing and Computational Science and Engineering Faculty Fellow, and Professor in the Department of Electrical and Computer Engineering, Boston University. His research focuses on the development of tools for the specification, design, assembly, and test of synthetic biological systems. His approaches draw upon his experience with embedded system-level design and electronic design automation (EDA). Extracting concepts and methodologies from these fields, he aims to raise the level of abstraction in synthetic biology by employing standardized biological part-based designs which leverage domain-specific languages, constraint-based genetic circuit composition, visual editing environments, microfluidics, and automated DNA assembly. This leads to a new research area he calls "Hardware, Software, Wetware Co-design".

Rabia Tugce Yazicigil (Senior Member, IEEE) received the Ph.D. degree from Columbia University, in 2016. She is an Assistant Professor with ECE Department, Boston University and a Network Faculty with Sabanci University. She was a Postdoctoral Associate with MIT. Her research interests lie at the interface of integrated circuits, bio-sensing, signal processing, security, and wireless communications to innovate system-level solutions for future energy constrained applications. She has received numerous awards, including the NSF CAREER Award (2024), Early Career Excellence in Research Award for the Boston University College of Engineering (2024), the Catalyst Foundation Award (2021), Boston University ENG Dean Catalyst Award (2021), and "Electrical Engineering Collaborative Research Award" for her Ph.D. research (2016). She is an Active Member of the Solid-State Circuits Society (SSCS) Women-in-Circuits Committee and is a member of the 2015 MIT EECS Rising Stars cohort. She was selected as an IEEE SSCS Distinguished Lecturer for the 2024–2026 term and elected to the IEEE SSCS AdCom as a Member-at-Large in 2024. She was selected as a member of the 2024 National Academy of Engineering (NAE) US Frontiers of Engineering (USFOE) cohort. She serves as an Associate Editor of IEEE TRANSACTIONS ON CIRCUITS AND SYSTEMS-I (TCAS-I) and IEEE TRANSACTIONS ON CIRCUITS AND SYSTEMS FOR ARTIFICIAL INTELLIGENCE (TCASAI). Additionally, she is the Workshop Co-Chair of the IEEE ESSERC 2024, and a Technical Program Committee member of the IEEE ISSCC, RFIC, and DAC.